Colloidal deposits from evaporating sessile droplets: Coffee ring versus surface capture

Nathan C. J. Coombs[*] and James E. Sprittles[†]
Mathematics Institute, University of Warwick, Coventry, CV4 7AL, United Kingdom

Mykyta V. Chubynsky[‡]
Research Centre for Fluid and Complex Systems, Coventry University, Coventry, CV1 2NL, United Kingdom

(Received 7 November 2023; accepted 23 May 2024; published 11 June 2024)

Suppression of the coffee ring effect is desirable in many industrial applications which utilize colloidal deposition from an evaporating liquid. Here we focus on the role of particle arrest at the liquid-air interface (surface capture) which occurs at high evaporation rates. It is known experimentally that this phenomenon inhibits particles from reaching the contact line, leading to a deposit which is closer to uniform. We are able to describe this effect using a simple 1D modeling framework and, utilizing asymptotic theory, parametrize our model by the ratio of the vertical advection and diffusion timescales. We show that our model is consistent with existing frameworks for small values of this parameter, but also predicts the surface layer formation seen experimentally at high evaporation rates. The formation of a surface layer leads to a deposit morphology which mimics the evaporative flux density and so is closest to uniform when evaporation has a constant strength across the liquid-air interface.

DOI: 10.1103/PhysRevFluids.9.064304

I. INTRODUCTION

The *coffee ring effect* (CRE), referring to the accumulation of solute particles near the contact line of an evaporating sessile droplet, is a ubiquitous phenomenon routinely seen in our daily lives and arising in numerous industrial settings. Some examples include inkjet printing [1], dip coating [2] and DNA alignment in optical gene mapping [3]. The underlying physical mechanism driving coffee ring formation has been well understood since the 1997 exposition of Deegan *et al.* [4] and was described in a recent review by Gelderblom *et al.* [5]: capillary flow arises in the droplet bulk due to the mismatch between the local evaporation flux density and the geometrical constraint enforced by the droplet's minimal surface energy shape and the pinned contact line. This capillary flow carries particles towards the contact line where an enhanced deposit is observed. Despite the simple physical explanation for the CRE, the dynamics of drying particle suspensions can be rich and complex. For example, Yabu and Shimomura [6] report a regular stripe patterned deposit left behind by the receding meniscus during the casting of polymer films; shear bands resembling chevrons [7], fracture patterns [8] and buckling instabilities [9,10] have also been observed.

[*]Contact author: Nathan.Coombs@warwick.ac.uk
[†]Contact author: J.E.Sprittles@warwick.ac.uk
[‡]Contact author: ae2173@coventry.ac.uk

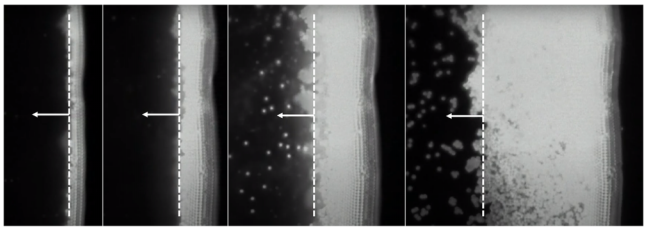

FIG. 1. An advancing front of jammed particles which are accumulating near the contact line of a sessile evaporating droplet. Extracted from a video in Ref. [12].

In this article, particular attention will be given to the effects of finite particle size; these are often neglected in CRE models, yet are experimentally often crucial. At high enough solute volume fractions (typically around the close packing efficiency of randomly distributed monodisperse spherical particles, 64%), the solute undergoes a transition towards a porous solid. We will refer to this effect as *jamming* [11]. Particles approaching the jamming threshold become immobile (i.e., they are no longer freely advected by the fluid). Using colloids of size $\approx$1 μm, optical microscopy experiments by Marín *et al.* [12] allow for direct observation of this phenomenon (see Fig. 1). These experiments have also revealed that the jammed deposit can exhibit both ordered and disordered phases depending on the particle advection speed: slowly advected particles have more time to arrange into an optimal packing structure and vice versa. The deposit is also found experimentally to be incompressible [13,14], meaning interactions between the liquid-air interface and the newly formed deposit must be accounted for during evaporation. We note that, prior to jamming, particles may also aggregate and form clusters due to the presence of van der Waals forces or liquid bridges. For simplicity, we shall neglect aggregation and assume that particle arrest happens due to jamming throughout this article.

From a modeling perspective, inclusion of jamming is important for obtaining coffee ring profiles with a realistic thickness. If particles are assumed passive in the fluid, with only diffusion balancing advective transport, then the particle concentration at the contact line rises without bound and the ring thickness decreases in width with time down to a line [15], in direct contrast with observation. To go beyond these models, one must capture the change in fluid and particle dynamics in the growing region of jammed solute. The fluid flow through the porous solid, which exists to compensate for evaporative losses in this region, is well described by Darcy's law [16,17].

Experimentally, it is possible to calculate the rate of mass loss of an evaporating droplet by weighing it throughout the drying process. If the droplet's dimensions are known, we can then use this to estimate the surface-averaged evaporation flux density $\mathcal{J}^*$ (i.e., the rate of mass loss per unit surface area). Assuming $\mathcal{J}^*$, the droplet radius R^*, and solutal diffusion coefficient D^* are known, three parameters will be of importance in this study [note that here and throughout the rest of this article an asterisk (*) is used to indicate a dimensional quantity]:

(i) ϵ: The drop's initial aspect ratio (height to radius).

(ii) $\mathrm{Pe} = R^*\mathcal{J}^*/\epsilon\rho^*D^*$: The Péclet number, quantifying advection against diffusion.

(iii) ϕ_c: The solute volume fraction at jamming.

The simplest modeling framework capable of qualitatively reproducing CRE dynamics assumes the drop to have a low aspect ratio and a vertically homogeneous solute distribution [15,16,18,19]. This allows for a formulation in terms of depth-averaged quantities, reducing the number of dimensions and hence overall complexity of the model; this is particularly important for reducing the cost of computing fully 3D profiles (e.g., printed lines). Since the ring is formed primarily by particle advection and jamming, it is also convenient to neglect lateral diffusion. Formally, these assumptions are equivalent to the asymptotic limit [20]:

$$\epsilon \ll 1, \quad \mathrm{Pe} \gg 1, \quad \epsilon^2\mathrm{Pe} \ll 1. \tag{1}$$

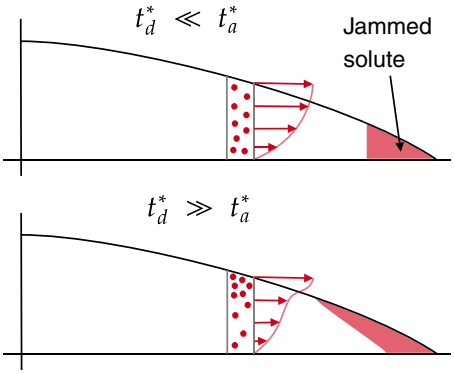

FIG. 2. A schematic representing the vertical particle distributions and jammed regions for differing timescales t_a^* and t_d^*. Arrows represent radial mass fluxes (vertical fluxes are not shown). When $t_a^* \ll t_d^*$, the solute is vertically homogeneous, and so the jammed deposit has a vertical front. When $t_d^* \gg t_a^*$ the solute is more concentrated near the free surface, and so the jammed deposit exhibits an overhang.

Depending on the evaporation strength and particle size (influencing the solutal diffusion coefficient), the Péclet number for this problem can vary across orders of magnitude. Fortunately, the limit given above is applicable to a wide range of particle suspensions (see examples given in Sec. II). Theoretical work by Larsson and Kumar [21] even suggests that this assumption retains accuracy if ϵ^2Pe is of order unity or larger, an observation which is consistent with our findings in Sec. V B. Asymptotic approximations strike a balance between complexity and accuracy in allowing for simple analytic expressions for the evaporation-induced capillary flow that hold up reasonably well against experimental data [12,22].

In most applications CRE is undesirable. In the field of inkjet-printed electronics, for instance, a reduced deposit in the interior limits the mobility of charge carriers and thus lowers the overall conductivity. This has motivated a range of studies into control via electrostatic suppresssion [18], manipulating particle shape [23] and the Marangoni effect [24], to give examples. Another candidate for CRE suppression, which has been studied less extensively, occurs at large evaporation rates. In this limit, the timescale associated with vertical advection $t_a^* = \rho^* \epsilon R^* / \mathcal{J}^*$ is much shorter than the timescale for vertical dispersion $t_d^* = \epsilon^2 R^{*2} / D^*$ so particles adhere to the retreating liquid-air interface before they can escape via diffusion [25–27] (see Fig. 2). In this article we will refer to this adhesion phenomenon at the free surface as *surface capture*, though other naming conventions exist (the surface particle layer is often referred to as a "skin" [28,29]).

Li *et al.* [26] found that, through the surface capture mechanism, the dried deposit morphology is much closer to uniform (the observed deposits can be found in Sec. V A and have been compared to our predictions). The result holds for mono- and polydisperense nanoparticles across a range of sizes. Though there have been theoretical studies which recognize surface capture [30,31], to the authors' knowledge there is no existing model that successfully incorporates both jamming and surface capture effects (with the notable exception of Maki and Kumar [28], who modeled surface capture by simulating the full 2D axisymmetric advection diffusion equation in the drop), both of which are essential to predicting the coffee ring thickness, the extent of the surface layer, and the overall deposit morphology. Here we attempt to remedy this by lifting a number of assumptions in existing CRE models.

The model developed in Secs. II, III, and IV utilizes the hydrodynamic approach taken by Popov [19] (summarized in Sec. III): the lubrication equations are used to describe the bulk fluid flow and the free surface attains a minimal surface energy shape. In Popov's framework, particles are either freely advected with the fluid or jammed; there is no intermediate "slurry" region as considered by Kaplan and Mahadevan [17], for instance. In Sec. IV A we will first examine the pure surface capture

regime in which diffusion is neglected entirely and so particles are transported along streamlines until they terminate at the jammed surface layer/contact line deposit. This regime is defined formally by the limit

$$\epsilon \ll 1, \quad \mathrm{Pe} \gg \epsilon^2 \mathrm{Pe} \gg 1. \tag{2}$$

Following this, we will look into intermediate cases: By specifying the vertical concentration profile *a priori* with a diffusive boundary layer expression parameterized by ϵ^2Pe, in Sec. IV C we will develop a more general model that retains the low-dimensional character of the conventional CRE models (a feature which is so far not present in models of surface capture). This framework is consistent with Popov's model and pure surface capture in the limits given by (1) and (2), respectively. Additional information on the existence/radial extent of the jammed surface layer can be found at intermediate ϵ^2Pe.

II. EVAPORATION DYNAMICS

As we will see, the functional dependence of the evaporative flux density will have a strong influence on the deposit morphology, particularly towards the surface capture regime. It is therefore worth discussing the evaporation dynamics in depth. In CRE literature, it is common to assume one of two expressions for the local evaporation flux density J^*_{evap} [15,19,32,33]:

(i) *Kinetic evaporation:*

$$J^*_{\mathrm{evap}} = \mathcal{J}^*_k \tag{3}$$

(ii) *Diffusive evaporation:*

$$J^*_{\mathrm{evap}} = \frac{1}{2}\frac{\mathcal{J}^*_d}{\sqrt{1-(r^*/R^*)^2}}, \tag{4}$$

where $\mathcal{J}^*_k$, $\mathcal{J}^*_d$ are constants and R^* is the droplet radius. Each of these models represents a rate-limiting step in the evaporation process. For kinetic evaporation it is assumed that the liquid-vapor phase transition is rate-limiting, whereas for diffusive evaporation the dispersion of saturated vapor adjacent to the free surface is rate limiting. The diffusive evaporation model also assumes both the droplet aspect ratio $\epsilon \to 0$ and the surrounding air to be quiescent, meaning the drop and the air must be in thermal equilibrium. Equation (4) is then obtained by solving the quasisteady diffusion problem for the solvent vapor above the drop [34].

Experimentally, one might control the drop temperature by heating the substrate. This inevitably gives rise to thermal convection in the surrounding air [35]. Convection currents can act to carry saturated vapor away from the liquid-air interface, leading to a larger global evaporation rate than would be expected if diffusion were dominant. Through this mechanism, convection may also cause local variations in the evaporation flux, giving an evaporation profile which is closer to uniform as seen the kinetic regime. Even under isothermal conditions, the diffusive evaporation model neglects Stefan flow, which arises due to the differences in density between the saturated vapor at the droplet surface and surrounding air.

Neglecting the aforementioned effects, in the diffusive case, the evaporation strength can be written as [19,34]

$$\mathcal{J}^*_d = \frac{4}{\pi}\frac{D^*_{\mathrm{air}}(\Phi^*_0 - \Phi^*_\infty)}{R^*}, \tag{5}$$

where Φ^*_0, Φ^*_∞ are the saturation and far-field vapor densities and D^*_{air} is the vapor diffusion coefficient. Using $\mathcal{J}^*_d$ in place of $\mathcal{J}^*$, the Péclet number in terms of these parameters is thus $\mathrm{Pe} = (4/\pi)D^*_{\mathrm{air}}(\Phi^*_0 - \Phi^*_\infty)/\epsilon\rho^* D^*$. To demonstrate the applicability of the $\mathrm{Pe} \gg 1$ limit taken here, consider the case of the PEDOT:PSS complex, which is currently of interest in the field

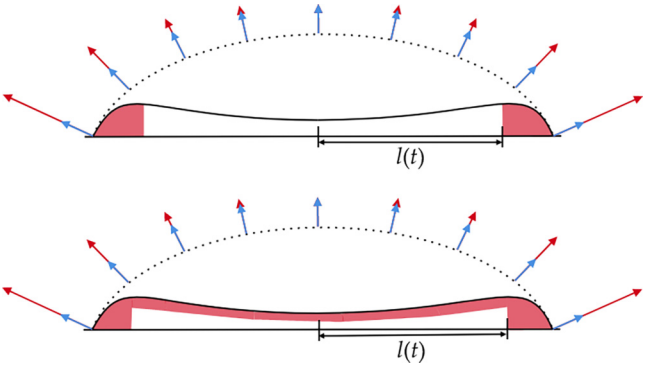

FIG. 3. A schematic of the drop shapes and the beginning (dotted line) and late (solid line) stages of evaporation. The jammed solute is depicted in pink to show its influence on the free surface height. In the upper figure there is only a coffee ring deposit, whereas in the lower figure a jammed surface layer has also formed. The kinetic and diffusive evaporation regimes are shown in blue and red, respectively.

of inkjet-printed electronics [36,37]. Assuming the printing medium is predominantly water, $\Phi_0^* - \Phi_\infty^* = 0.014\,\mathrm{kg\,m^{-3}}$ (given a humidity of 40%) [38] and $D_{\mathrm{air}}^* = 2.4 \times 10^{-5}\,\mathrm{m^2\,s^{-1}}$ [39] at room temperature. The PEDOT:PSS complex typically has a diameter of 16 nm [40], so application of the Stokes-Einstein relation gives $D^* \approx 3 \times 10^{-11}\,\mathrm{m^2\,s^{-1}}$. Hence, assuming an aspect ratio of $\epsilon \approx 0.3$, the Péclet number is $\mathrm{Pe} \approx 46$. Note also that as the solvent evaporates, the relative strength of advection to diffusion increases, and so the effective Péclet number increases with time. Repeating the calculation at a temperature of 75 °C (at which we expect surface capture effects to become more important) while retaining a humidity of 40% gives $\mathrm{Pe} \approx 254$. Larger colloids with sizes ranging from hundreds of nanometres to microns have smaller diffusion coefficients, and so we expect the Péclet number for these suspensions to be larger still. Thus, the asymptotic limits used in this study, limits (1) and (2), are applicable to a wide range of suspensions.

III. FLUID DYNAMICS

We will begin by discussing the hydrodynamic component of our model. We assume that particles affect fluid flow only when they have jammed, so that the hydrodynamic problem is coupled to the solute concentration only through boundary conditions (i.e., the position of the jammed particle front). The following notation is utilized for depth averages:

$$\langle f(r^*, z^*, t^*)\rangle_g = \frac{1}{g}\int_0^g f(r^*, z^*, t^*)\,dz^*\,. \tag{6}$$

If no subscript g is specified, integration up to the liquid-air interface $z^* = h_{\mathrm{tot}}^*$ is implied. We will also make reference to averages up to the height of the bottom of the surface layer, $z^* = b^*$, where relevant.

The expected dynamics are depicted in Figs. 3 and 4. From the moment evaporation begins, there appears a region near the contact line occupied by jammed solute. A sharp "shock" front separates this region and the region of free advection. As evaporation progresses, the free surface height decreases and the contact line deposit grows in thickness. Since this deposit is incompressible, the surface cannot recede any further where it has formed. Depending on the system parameters, we may also see solute jamming at the liquid-air interface. Ultimately, as the deposit region grows, we see a reversal in curvature of the free surface at the later stages of evaporation, followed by either the free surface or the jammed surface layer meeting the substrate at $r^* = 0$ (lower left and lower right panels in Fig. 4 respectively). In theoretical studies by Popov [19] and Kaplan and Mahadevan [17] (both of which take the vertically homogeneous limit), the post-touchdown dynamics are omitted

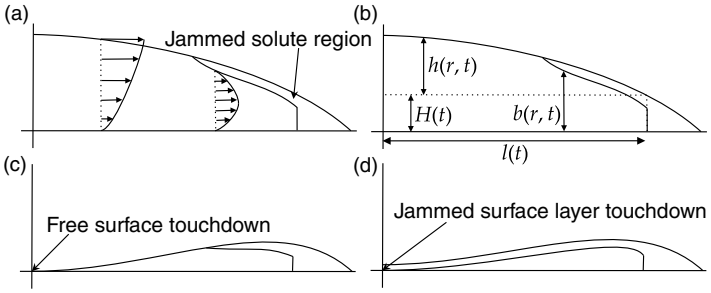

FIG. 4. Schematics describing aspects of the model. The arrows in (a) depict the transition from a semi- to full-Poiseuille flow in the presence of a jammed surface layer. Panel (b) depicts the variables describing the drop geometry, contact line deposit, and surface layer. Panels (c) and (d) show two distinct possibilities at the later stages of evaporation: touchdown of the free surface or jammed surface layer.

since the modeling frameworks used by both break down at this stage. We will also omit this stage. However, our related article [41] includes post-touchdown behavior in the context of a different modeling framework.

Since the drop has a low aspect ratio, $\epsilon \ll 1$, the fluid flow is well modeled by the lubrication equations [15,16,42]

$$\frac{\partial h_{\text{tot}}^*}{\partial t^*} + \frac{1}{r^*}\frac{\partial}{\partial r^*}(r^*\langle u^*\rangle h_{\text{tot}}^*) + J_{\text{evap}}^*/\rho^* = 0, \tag{7a}$$

$$\langle u^*\rangle = -\frac{\Gamma^*}{\mu^*}\frac{\partial p^*}{\partial r^*}, \tag{7b}$$

$$p^* = p_{\text{atm}}^* - \frac{\sigma^*}{r^*}\frac{\partial}{\partial r^*}\left(r^*\frac{\partial h_{\text{tot}}^*}{\partial r^*}\right), \tag{7c}$$

where p^* is the pressure, u^* is the radial fluid velocity, and ρ^*, μ^*, and σ^* are the fluid density, dynamic viscosity, and surface tension, respectively. The precise form of the prefactor Γ^* is not important here. However, given the modeling assumptions made in subsequent sections, it will take the form of either ${h_{\text{tot}}^*}^2/3$ or ${b^*}^2/12$, depending on whether a surface layer has formed or not. Since the fluid flow is evaporation-induced, the scale for radial velocity is $U^* = \mathcal{J}^*/\rho^*\epsilon$. The capillary number is thus $\text{Ca} = \mu^* U^*/\sigma^* = \mu^*\mathcal{J}^*/(\rho^*\sigma^*\epsilon)$. The nondimensionalization which we will use for the rest of this study is

$$\begin{aligned} &r^* = R^* r, \quad z^* = \epsilon R^* z, \quad J_{\text{evap}}^* = \mathcal{J}^* J_{\text{evap}}, \quad \langle u^*\rangle = U^*\langle u\rangle, \\ &t^* = \frac{R^*}{U^*}t_f t, \quad p^* - p_{\text{atm}}^* = \frac{\mu^* U^*}{\epsilon^2 R^*}p, \quad h_{\text{tot}}^* = \epsilon R^* h_{\text{tot}}, \\ &b^* = \epsilon R^* b, \quad \Gamma^* = \epsilon^2 {R^*}^2\Gamma, \end{aligned} \tag{8}$$

where t_f is an $O(1)$ parameter to be later assigned for convenience. The dimensionless governing equations then become

$$\frac{1}{t_f}\frac{\partial h_{\text{tot}}}{\partial t} + \frac{1}{r}\frac{\partial}{\partial r}(r\langle u\rangle h_{\text{tot}}) + J_{\text{evap}} = 0, \tag{9a}$$

$$\langle u\rangle = -\Gamma\frac{\partial p}{\partial r}, \tag{9b}$$

$$p = -\frac{1}{\widetilde{\text{Ca}}}\frac{1}{r}\frac{\partial}{\partial r}\left(r\frac{\partial h_{\text{tot}}}{\partial r}\right), \tag{9c}$$

where $\widetilde{\mathrm{Ca}} = \mathrm{Ca}/\epsilon^3$ is a scaled capillary number. Experimental droplet evaporation studies by Brutin [43] quote a typical drop radius of $R^* = 1.8\,\mathrm{mm}$ and a global evaporation rate (per unit drop radius) of $E^* = 1.6\,\mathrm{mg\,s^{-1}\,m^{-1}} \sim \pi R^* \mathcal{J}^*$. Even with an aspect ratio of $\epsilon = 0.1$, lower than what is seen experimentally at the start of the drying process according to contact angle measurements, the resulting scaled capillary number is $\widetilde{\mathrm{Ca}} = 3.5 \times 10^{-5}$, implying that the limit $\widetilde{\mathrm{Ca}} \ll 1$ will be applicable throughout most of the drying process. We are thus justified in performing the asymptotic expansion:

$$h_{\mathrm{tot}} = h_{\mathrm{tot},0} + \widetilde{\mathrm{Ca}}\, h_{\mathrm{tot},1} + \cdots ,$$

it is readily found that

$$\frac{\partial}{\partial r}\left[\frac{1}{r}\frac{\partial}{\partial r}\left(r\frac{\partial h_{\mathrm{tot},0}}{\partial r}\right)\right] = 0. \tag{10}$$

This equation can be integrated three times. Since we require a nonsingular solution at $r = 0$, there will be two degrees of freedom to specify after integration.

Following Popov, it is convenient to split the free surface height into the contributions $h_{\mathrm{tot}} = h(r,t) + H(t)$, as indicated in Fig. 4(a). Regardless of whether a surface layer has formed or not, $H(t)$ represents the height of the jammed deposit at the jamming shock front. We will assume that the jammed solute is an incompressible porous solid. When jammed particles do not span the drop thickness, they move vertically with the free surface but not horizontally. Once jammed particles span the entire thickness of the drop the deposit becomes stationary. The latter of these regimes occurs on the domain $r \in [l(t), 1]$, where $l(t)$, the position of the shock front, is to be found. Since the $\partial h_{\mathrm{tot}}/\partial t = 0$ beyond the shock front, the jammed solute continuously repins the drop. After integrating Eq. (10) and applying the boundary condition $h(l(t), t) = 0$, we have

$$h_{\mathrm{tot},0} = A(l^2 - r^2) + H, \tag{11}$$

where A is time-dependent. An additional condition, verified experimentally by Deegan [44], is that the free surface gradient should be continuous at $r = l(t)$:

$$\left.\frac{\partial h_{\mathrm{tot},0}}{\partial r}\right|_{r=l} = -2Al = \left.\frac{d}{dr}\right|_{r=l} H(l^{-1}(r)) = \frac{\dot{H}}{\dot{l}}$$
$$\longrightarrow \dot{H} = -2Al\dot{l}, \tag{12}$$

where $l^{-1}(r)$ is the inverse function of l and so is the time at which the shock front passes through position r. To find another component equation of our system, we look at the global mass balance (solvent and solute), which states that the rate of change of the total droplet mass must be equal to evaporative losses:

$$\frac{1}{t_f}\frac{d}{dt}\left\{\int_0^l r h_{\mathrm{tot},0}\, dr + \int_0^t |(Hl\dot{l})(t')|\, dt'\right\} = \frac{\dot{A}l^4}{4t_f} = -\int_0^1 r J_{\mathrm{evap}}\, dr\,. \tag{13}$$

The second term on the left side of this expression is the mass in the deposit phase [i.e., $r > l(t)$ so excluding the surface layer], which grows by an amount $|Hl\delta l|$ over time δt. Note that in this equation we are implicitly assuming that the densities of the solvent and solute are equal and that the jammed region remains saturated with solvent throughout drying. This latter assumption is supported by the fact that the mass of the drop changes linearly through most of the drying process [44]. We are also assuming that jammed particles at the surface do not impede evaporation. Under diffusive evaporation, this assumption is likely to remain valid as long as the jammed regions are saturated, since the evaporation rate is determined by the vapor distribution in the gas phase and the Dirichlet boundary condition for the vapor concentration on the drop surface, $\Phi^* = \Phi_0^*$, is still a good approximation even when jammed particles are present. Therefore the quasisteady diffusion problem from which Eq. (4) is derived would be unchanged. Under kinetic evaporation, particles

near the drop surface may impede evaporation as there is a reduced surface area available for the liquid-vapor phase transition. Thus, in this regime we may expect the evaporation rate to be reduced by a factor of $(1-\phi)|_{z=h_{\rm tot}}$ [45]. Such a reduction is unlikely to make a significant difference to our results in limits (1) and (2), as in the former limit the jammed region occupies only a small region near the contact line (meaning the global evaporation profile is nearly unchanged) and in the latter limit jammed particles span the entire drop surface, so the evaporation profile is still uniform. Therefore, it is likely that while particles impeding evaporation would affect the dynamics of surface layer formation, our results would remain qualitatively unchanged.

As noted above, diffusive evaporation in presence of thermal convection currents can lead to $J_{\rm evap}$ profiles that mimic the kinetic case. Therefore, at least as far as this case is concerned, our assumption that $J_{\rm evap}$ is independent of that local solute concentration remains valid. Of course, unimpeded evaporation in the jammed regions is possible only if the capillary pressure is large enough to force the solute through the porous deposit. We refer the reader to Routh and Russel [16] for an in-depth analysis and justification of this assumption.

For completeness, and to determine the most appropriate timescale in this problem, it is worth looking at the case in which there is no particle jamming. Clearly in this case we will always be in the pre-touchdown regime with $H=0$, $l=1$. The global mass balance then becomes

$$\frac{\dot{A}}{4t_f} = -\int_0^1 rJ_{\rm evap}\,dr = -\frac{1}{2}, \tag{14}$$

for both kinetic and diffusive evaporation. It is convenient to scale our time coordinate so that dry-out is achieved at $t=1$. This requires that we set $t_f=\frac{1}{2}$. It is worth noting, however, that with jamming present $t=1$ will not necessarily represent the true dry-out time, as post-touchdown there may be complications such as film de-wetting processes. Since in our model the jammed regions remain saturated with solvent at all times, it is unclear how to define true dry-out. A sensible definition might be the time at which $\phi=\phi_c$ everywhere so that the suspension is incompressible everywhere and no further deformation can take place. This issue will be addressed in future work.

With our chosen values of t_f, the solvent balance condition becomes

$$\dot{A}l^4 = -1, \tag{15}$$

regardless of which evaporation model we are using.

The next step in our analysis is to find the depth-averaged radial velocity profile. As this quantity is derived directly from the continuity equation for the fluid, it will be the same whether there is any surface jamming or not. Again following Popov, we have

$$\langle u\rangle = (rh_{\rm tot})^{-1}\left\{\frac{1}{t_f}\left[\frac{1}{2}\left(\frac{r}{l}\right)^2 - \frac{1}{4}\left(\frac{r}{l}\right)^4\right] - \int_0^r r'J_{\rm evap}(r')\,dr'\right\}. \tag{16}$$

Though it is not needed in our model, the exact z dependence of the velocity in the presence of a surface layer can be inferred through simple physical arguments. In a porous solid the fluid flow is described by Darcy's law: $\nabla^* p^* = -(1/k^*)(\boldsymbol{u}_f^* - \boldsymbol{u}_s^*)$, where k^* is the permeability and $\boldsymbol{u}_f^*$, $\boldsymbol{u}_s^*$ are the fluid (solvent) and solute velocities, respectively. Thus, the pressure obeys Laplace's equation, $\nabla^{*2} p^* = 0$, in the surface layer. Given this and the fact that the pressure at the top of the jammed layer is equal to the atmospheric pressure, the pressure drop across the surface layer is at least of the same order of magnitude as along it. Letting Δp^* denote this pressure drop, we see that the scales for the radial and vertical velocities are $U^* = k^*\Delta p^*/R^*$ and $W^* = k^*\Delta p^*/\epsilon R^*$ respectively, meaning when ϵ is small the flow is predominantly vertical. Hence, if $b(r,t)$ represents the height of the jammed surface layer, the relevant boundary condition at $z=b$ is $u=0$. This means that there is a transition from a free surface flow to a Poiseuille flow where the surface layer has formed (see the left of Fig. 4 for reference). It is worth emphasizing that the derivation of this boundary condition is the only application of Darcy's law in our model. Since the geometry of

our problem is axisymmetric, fluid and particle fluxes may be obtained directly from the relevant transport equations without ever needing to solve for the pressure distribution.

So far we have two consitutive equations [(12) and (15)] for our system comprising A, H, l and the solute volume fraction ϕ. These are two of the equations originally derived by Popov. The remaining two are limited to vertically homogeneous suspensions and thus require modification. To close our system, we must first examine the particle transport dynamics.

IV. PARTICLE TRANSPORT

Neglecting any surface layer for the moment, particle transport in our system is modeled according to an advection-diffusion equation:

$$\frac{\partial \phi}{\partial t^*} + \frac{1}{r^*}\frac{\partial}{\partial r^*}\left[r^*\left(u_a^*\phi - D^*\frac{\partial \phi}{\partial r^*}\right)\right] + \frac{\partial}{\partial z^*}\left[w_a^*\phi - D^*\frac{\partial \phi}{\partial z^*}\right] = 0, \tag{17}$$

where u_a^* and w_a^* are the radial and vertical advective velocity components, respectively (equal to the the solvent velocity prior to jamming) and D^* is the solutal diffusion coefficient mentioned earlier. In general D^* and the suspension viscosity μ^* may be ϕ-dependent [46]. In particular, if particles aggregate and form clusters before jamming, this would result in an increase in the effective particle size and hence a reduction in the diffusion coefficient. Consequently, jamming would occur more readily among these aggregates, and so the expected time taken for surface layer to form, as discussed in Sec. IV B, for instance, would decrease. Beyond this effect, however, we expect such dependencies to make little difference to our results as we will be neglecting horizontal diffusion and most of the constitutive equations of our model are a direct consequence of mass conservation. For instance, the fluid velocity (which is the velocity of both the solute and solvent in our model) is determined via direct integration of the continuity equation, and so any variations in viscosity are irrelevant. In dimensionless variables, with $(u_a^*, w_a^*) = U^*(u_a, \epsilon w_a)$, Eq. (17) reads

$$\frac{1}{t_f}\frac{\partial \phi}{\partial t} + \frac{1}{r}\frac{\partial}{\partial r}[r u_a \phi] + \frac{\partial}{\partial z}\left[w_a\phi - \frac{1}{\epsilon^2 \mathrm{Pe}}\frac{\partial \phi}{\partial z}\right] = 0, \tag{18}$$

with the Péclet number as introduced in Sec. I. Note that the radial diffusion term is omitted since we will always be assuming the $\mathrm{Pe} \gg 1$ limit. In particular, there is no need for a finite radial Péclet number in this setting since the coffee ring forms through jamming rather than the balance of advection and diffusion, as considered elsewhere [15,47]. It is also worth noting that the advection strength increases with decreasing drop height, and so we expect this approximation to become better further into the evaporative process.

Accounting for interface motion, the no-flux condition at the liquid-air interface $z = h_{\mathrm{tot}}$ is

$$\left[\left(\frac{1}{t_f}\frac{\partial h_{\mathrm{tot}}}{\partial t} + u_a\frac{\partial h_{\mathrm{tot}}}{\partial r} - w_a\right)\phi + \frac{1}{\epsilon^2 \mathrm{Pe}}\frac{\partial \phi}{\partial z}\right]_{z=h_{\mathrm{tot}}} = 0. \tag{19}$$

It will be instructive to combine this condition with the kinematic boundary condition on the bulk fluid, which reads

$$\left[\frac{1}{t_f}\frac{\partial h_{\mathrm{tot}}}{\partial t} + u_a\frac{\partial h_{\mathrm{tot}}}{\partial r} - w_a\right]_{z=h_{\mathrm{tot}}} + J_{\mathrm{evap}} = 0$$

$$\longrightarrow \left[\frac{1}{\epsilon^2 \mathrm{Pe}}\frac{\partial \phi}{\partial z} - J_{\mathrm{evap}}\phi\right]_{z=h_{\mathrm{tot}}} = 0. \tag{20}$$

When expressed in this way we can intuitively picture how vertical concentration gradients are affected by the local evaporation strength.

The rest of this section will be organized as follows: First, we will examine the $\epsilon^2 \mathrm{Pe} \gg 1$ asymptotics in the case of a flat interface. Motivated by these results and the consistency of the boundary condition with Eq. (20), we will propose a 1D interpolation between the surface capture

and vertically homogeneous regimes which is consistent with these limits but also provides some insight into the intermediate cases.

A. The surface capture limit

Since the $\epsilon^2 \mathrm{Pe} \ll 1$ limit in our model simply gives the results outlined by Popov [19], we examine the opposite limit, $\epsilon^2 \mathrm{Pe} \gg 1$, in which diffusion is not present at all in the bulk.

The model setup will be similar to that outlined in Fig. 4, except the jammed layer spans the free surface instantaneously. With no diffusion present, the solute concentration is constant along streamlines (this is evident simply by combining the incompressibility condition with the advection equation). Thus, if we have $\phi(r, z, 0) = \phi_0$ initially, it will remain at this value everywhere in the bulk of the fluid, with particles concentrated at the boundaries such that the total solute mass is conserved. Thus, a sharp transition from ϕ_0 to ϕ_c occurs when the solute jams with no intermediate values. This means we have to solve only for b using the governing equation:

$$\frac{\phi_c - \phi_0}{t_f}\frac{\partial b}{\partial t} = \phi_0\left[u\frac{\partial b}{\partial r} - w\right]_{z=b} + \frac{\phi_c}{t_f}\frac{\partial h_{\mathrm{tot}}}{\partial t}. \tag{21}$$

This is obtained from Eq. (18) by noting that jammed particles in the surface layer move at a vertical velocity $w_a = t_f^{-1}\partial_t h_{\mathrm{tot}}$ and therefore using the substitutions $\phi = \phi_0\Theta(b - z) + \phi_c\Theta(z - b)$ and $(u_a, w_a) = (u, w)\Theta(b - z) + (0, t_f^{-1}\partial_t h)\Theta(z - b)$, where Θ is the Heaviside step function. It is worth noting that the assumption of jammed solute moving at the same velocity as the free surface can introduce problems with incompressibility if the surface area of the air liquid interface changes during evaporation. For example, in an experimental work by Pauchard and Allain [9] on the drying of polymer solutions it was found that the surface layer prevents changes surface area but does not impede evaporation, ultimately leading to buckling instabilities. Fortunately, the change in surface area is minimal for low aspect ratio drops, so this issue can be neglected. By integrating the incompressibility condition vertically up to $z = b$, we may write Eq. (21) as

$$\frac{\phi_c - \phi_0}{t_f}\frac{\partial b}{\partial t} = \frac{1}{r}\frac{\partial}{\partial r}[rb\langle u\rangle_b\phi_0] + \frac{\phi_c}{t_f}\frac{\partial h_{\mathrm{tot}}}{\partial t}. \tag{22}$$

There is a clear interpretation for each of the terms on the right-hand side. The first is due to advection of particles into the column at a given radial coordinate, the second is due to the receding surface sweeping through the bulk and picking up particles.

Note that for the advective term in (22) we can simply use the flux found via the continuity equation. This is because all the radial fluid flow compensating for evaporation occurs in the free region, as argued in Sec. III, meaning $b\langle u\rangle_b = h_{\mathrm{tot}}\langle u\rangle$. One caveat with this modeling assumption is that it is inconsistent with the treatment of the region where the layer spans the entire substrate. Clearly, radial flow must exist in this region to compensate for evaporative losses. There is thus a flow discontinuity in our model at $r = l(t)$. In order to satisfy global solute mass conservation in our model, we must allow b to approach zero discontinuously: $b(r = l(t)^-, t) > 0$. Hence, even in the surface capture limit, our model still has distinct surface layer and coffee ring deposit regions. With aid of the suspension's continuity equation (9a) we can integrate Eq. (22) directly from the initial condition $b(r, 0) = h_{\mathrm{tot}}(r, 0)$ to give

$$b(r, t) = h_{\mathrm{tot}}(r, t) - \frac{\phi_0}{\phi_c - \phi_0}J_{\mathrm{evap}}(r)t_f t. \tag{23}$$

Thus, the thickness of the jammed surface layer $h_{\mathrm{tot}} - b$ grows linearly with time and has a spatial profile which mimics the evaporative flux density. This simple observation tells us that the kinetic evaporation limit is most likely to yield uniform deposits, as most of the solute mass per unit area

comes from the surface layer. The shock propagation condition required to close this system is

$$\dot{l} = -\frac{\phi_0}{\phi_c - \phi_0} t_f \langle u \rangle_b \Big|_{r=l}. \tag{24}$$

In order to proceed to the general case of intermediate ϵ^2Pe values, we must now allow for z dependence in the concentration field that is neither uniform nor a step function, as found in the limiting cases.

B. Solutal diffusive boundary layer structure: Case of a flat interface

Before focusing on the droplet geometry, we will first examine the simpler case of a flat interface with spatially uniform evaporation. The $\epsilon^2\text{Pe} \gg 1$ asymptotic result in this geometry can be used to inform the more general model applied to an axisymmetric drop. If the height of this interface is prescribed as $h_{\text{tot}} = 1 - t$, then continuity requires that $t_f = 1/J_{\text{evap}}$. There are two regimes we must consider: (1) the development of a diffusive boundary layer when surface jamming has not yet occurred and (2) the propagation of a jammed surface layer once the jamming threshold has been reached. A numerical treatment of a similar problem, in which the elastic properties of the layer are also considered, can be found in Ref. [29]. We also refer the reader to Ref. [45] for an analysis similar to the one given here. Since there is no induced capillary flow in our current problem, Eq. (18) becomes a simple 1D diffusion equation:

$$J_{\text{evap}} \frac{\partial \phi}{\partial t} = \frac{1}{\epsilon^2\text{Pe}} \frac{\partial^2 \phi}{\partial z^2}. \tag{25}$$

Focusing initially on the pre-jamming regime, the associated boundary conditions are

$$\frac{1}{\epsilon^2\text{Pe}} \frac{\partial \phi}{\partial z} - J_{\text{evap}} \phi = 0, \quad z = h_{\text{tot}}, \tag{26a}$$

$$\frac{\partial \phi}{\partial z} = 0, \quad z = 0. \tag{26b}$$

When we introduce the new coordinates,

$$\tilde{z} = \epsilon^2\text{Pe} J_{\text{evap}} (h_{\text{tot}} - z), \qquad \tilde{t} = t, \tag{27}$$

then the governing PDE becomes

$$\frac{1}{\epsilon^2\text{Pe} J_{\text{evap}}} \frac{\partial \phi}{\partial \tilde{t}} = \frac{\partial \phi}{\partial \tilde{z}} + \frac{\partial^2 \phi}{\partial \tilde{z}^2}, \tag{28}$$

with the boundary conditions

$$\frac{\partial \phi}{\partial \tilde{z}} + \phi = 0, \quad \tilde{z} = 0, \tag{29a}$$

$$\frac{\partial \phi}{\partial \tilde{z}} = 0, \quad \tilde{z} = \epsilon^2\text{Pe} J_{\text{evap}} h_{\text{tot}}. \tag{29b}$$

When ϵ^2Pe is large, we can effectively consider condition (29b) as a boundary condition at $\tilde{z} \to \infty$ providing we are not too close to the end of evaporation, i.e., $1 - \tilde{t} \lesssim (\epsilon^2\text{Pe} J_{\text{evap}})^{-1}$. It can be shown that

$$\phi = \phi_0 [1 + (\epsilon^2\text{Pe} J_{\text{evap}} \tilde{t} - \tilde{z} + 1) e^{-\tilde{z}}] \tag{30}$$

is an exact solution to Eq. (28) which satisfies both boundary conditions and conserves particle number, but does not match the initial condition. This is the solution that the system approaches at large times; the effect of violating the initial condition decays with time over the negligible timescale $(\epsilon^2\text{Pe} J_{\text{evap}})^{-1}$. We note that the term $\phi_0(1 - \tilde{z})e^{-\tilde{z}}$ contributes significantly only when

$\tilde{z} \lesssim 1$. Thus, when $\tilde{z} \gg 1$ it can be neglected when compared to the ϕ_0 term. Likewise, when $\tilde{z} \sim 1$ the term $\phi_0 \epsilon^2 \mathrm{Pe} J_{\mathrm{evap}} \tilde{t} e^{-\tilde{z}}$ will dominate for times $t \gtrsim 1/(\epsilon^2 \mathrm{Pe} J_{\mathrm{evap}})$. We also note that the depth average $\langle (1-\tilde{z}) e^{-\tilde{z}} \rangle$ equates to 0, so neglecting this term does not introduce issues with particle conservation. Therefore, we will opt for the following approximate expression:

$$\phi = \phi_0 (1 + \epsilon^2 \mathrm{Pe} J_{\mathrm{evap}} \tilde{t}\, e^{-\tilde{z}}), \tag{31}$$

which now matches the initial condition. Switching back to original coordinates gives

$$\phi = \phi_0 + \phi_0 \epsilon^2 \mathrm{Pe} J_{\mathrm{evap}} t \exp[-\epsilon^2 \mathrm{Pe} J_{\mathrm{evap}} (h_{\mathrm{tot}} - z)]. \tag{32}$$

Once the jamming threshold has been reached, ϕ can not rise any further past ϕ_c. We thus have a jammed surface layer which propagates slightly faster than the speed of the free surface as a consequence of mass conservation. The Robin boundary condition at $z = h_{\mathrm{tot}}$ becomes a Dirichlet condition at $z = b$, so that

$$\phi = \phi_c, \quad z = b, \tag{33a}$$

$$\frac{\partial \phi}{\partial z} = 0, \quad z = 0. \tag{33b}$$

To solve for the extra variable b we must refer to the mass conservation condition:

$$0 = \frac{d}{dt} \int_0^b \phi \, dz + \phi_c \left(\frac{\partial h}{\partial t} - \frac{\partial b}{\partial t} \right). \tag{34}$$

Making a similar rescaling to Eq. (27), but replacing h_{tot} with b, we obtain

$$\frac{1}{\epsilon^2 \mathrm{Pe} J_{\mathrm{evap}}} \frac{\partial \phi}{\partial \tilde{t}} = -\dot{b} \frac{\partial \phi}{\partial \tilde{z}} + \frac{\partial^2 \phi}{\partial \tilde{z}^2}. \tag{35}$$

We will again seek a quasistationary solution, this time using the ansatz $\phi = \phi_0 + (\phi_c - \phi_0) \exp(\dot{b}\tilde{z})$, which is valid so long as $\dot{b}$ changes slowly. Substituting this expression into the mass conservation condition, we obtain the following equation for b:

$$\begin{aligned} 0 &= \int_0^b \frac{\partial \phi}{\partial t} \, dz - \phi_c \\ &= \frac{1}{\epsilon^2 \mathrm{Pe}\, J_{\mathrm{evap}}} \int_0^{\epsilon^2 \mathrm{Pe}\, J_{\mathrm{evap}} b} \left(\epsilon^2 \mathrm{Pe}\, \dot{b} \frac{\partial}{\partial \tilde{z}} + \frac{\partial}{\partial \tilde{t}} \right) [\phi_0 + (\phi_c - \phi_0) e^{\dot{b}\tilde{z}}] \, d\tilde{z} - \phi_c \approx -\dot{b}(\phi_c - \phi_0) + \phi_c. \end{aligned} \tag{36}$$

The final line in the equation above is obtained by first approximating the upper integration limit as $\epsilon^2 \mathrm{Pe}\, J_{\mathrm{evap}} b \to \infty$ and then neglecting all terms of order $(\epsilon^2 \mathrm{Pe}\, J_{\mathrm{evap}})^{-1}$ in the resulting expression. Matching the initial condition (i.e., the moment jamming occurs, at $t = t_c$) gives us

$$\phi = \phi_0 + (\phi_c - \phi_0) \exp\left[-\frac{\phi_c}{\phi_c - \phi_0} \epsilon^2 \mathrm{Pe} J_{\mathrm{evap}} (b - z) \right], \tag{37a}$$

$$b = 1 - \frac{\phi_c t - \phi_0 t_c}{\phi_c - \phi_0}, \tag{37b}$$

where $t_c = (\phi_c - \phi_0)/(\phi_0 \epsilon^2 \mathrm{Pe} J_{\mathrm{evap}})$ is the jamming delay time predicted by the theory in the pre-jamming regime. Figure 5 shows how this solution compares with the full numerical solution of equation (25) for $\epsilon^2 \mathrm{Pe} J_{\mathrm{evap}} = 50$. The axes are scaled appropriately to show collapse onto a universal curve predicted by the asymptotics. Clearly, if $\epsilon^2 \mathrm{Pe} < (\phi_c - \phi_0)/(\phi_0 J_{\mathrm{evap}})$ we will not see any surface layer formation at least until very late times, which are outside the range of applicability of the asymptotic solution due to the application of the boundary condition at $\tilde{z} \to -\infty$ being invalid. We will return to the significance of t_c in the general model. One caveat with the present analysis is that in switching from expression (31) to (37a), we introduce problems with solute mass

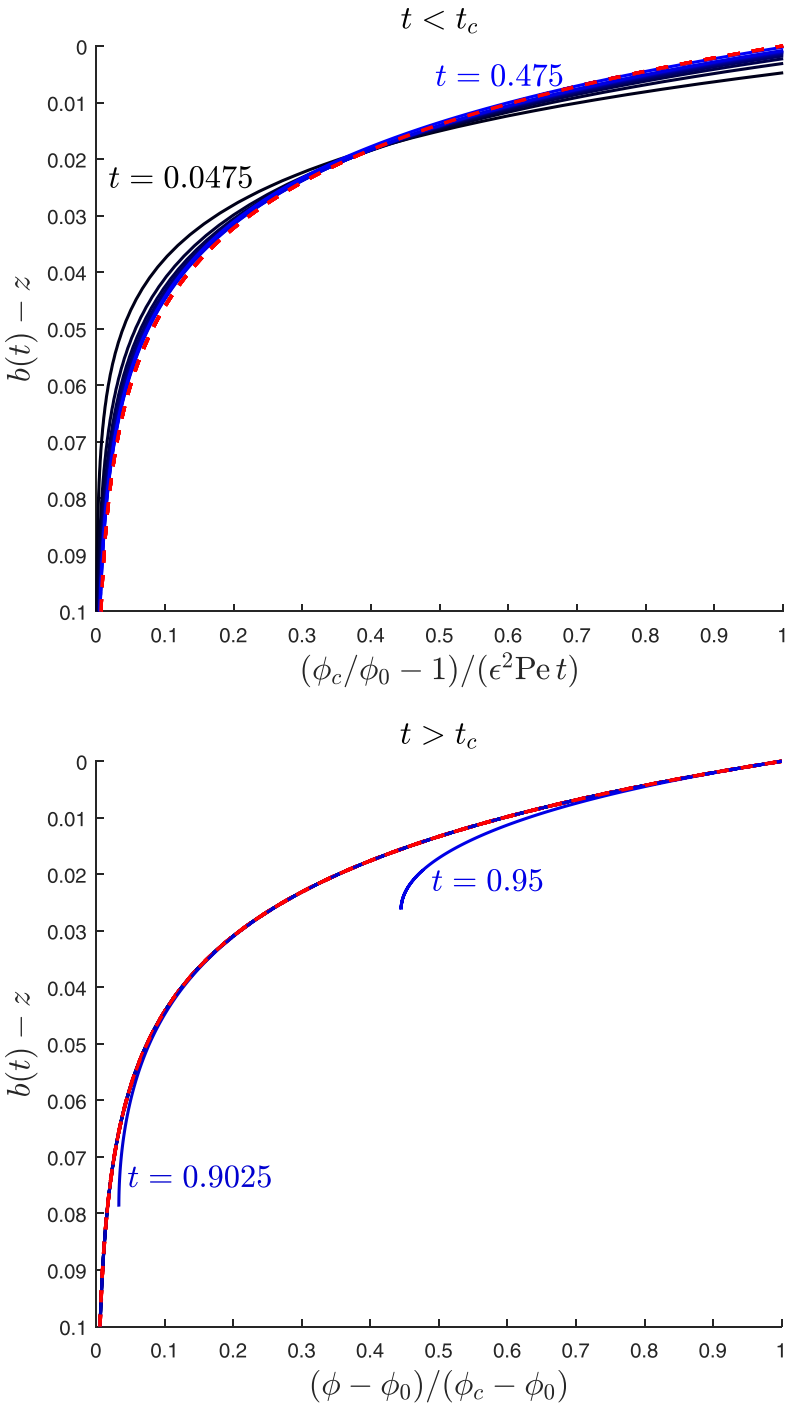

FIG. 5. Simulations of the 1D evaporation-diffusion problem with $\phi_c/\phi_0 = 25$ and $\epsilon^2 \mathrm{Pe} J_{\mathrm{evap}} = 50$, so that the jamming delay time is $t_c = 0.48$. In the lower panel, $b(t)$ has also been calculated numerically by coupling it to the concentration distribution using the relation $\dot{b} = -(\epsilon^2 \mathrm{Pe}\, J_{\mathrm{evap}})^{-1} (\partial_z^2 \phi)/(\partial_z \phi)|_{z=b}$. The top and bottom panels correspond to pre- and post-jamming, respectively. In each case the axes are appropriately scaled to show collapse onto a universal curve, as predicted by Eqs. (32) and (37).

conservation due to the instantaneous change in the exponential decay rate from 1 to $|\dot{b}|$. It was found from the direct simulations that the decay rate approaches $|\dot{b}|$ even before jamming is seen at the free surface, a feature which has not been accounted for in our analytical result. This discrepancy is negligible when $\phi_0/\phi_c \ll 1$, as will mostly be the case in this study. Nonetheless, one possible work-around is to allow for a nonphysical discontinuity in b when $t = t_c$, such that the overall particle number is conserved. Since the profile of ϕ is well captured by the solution ansatz in the post-jamming regime, introducing this discontinuity allows the b value predicted by the ansatz to "catch up" with the numerical result, so a good agreement between the two is seen thereafter. We have adopted this approach in the subsequent to section in order to ensure solute mass conservation in the simulations of the axisymmetric drop.

Note that, despite the presence of evaporation-induced fluid flow in the case of an axisymmetric drop, the boundary conditions (20) and (26a) are the same (since we are using a thin drop approximation). Based on this observation, we will use the results of this section to construct an ansatz for the z dependence of ϕ for the axisymmetric drop.

C. 1D interpolation between vertical homogeneity and surface capture

With the diffusive boundary layer structure established, we are in position to construct an interpolation model which captures both the vertically homogeneous dynamics at low values of ϵ^2Pe and surface layer formation at larger values. Regardless of the value of this parameter (ϵ^2Pe), the initial state will be the same: a uniform particle distribution in the bulk with no surface layer at all. The governing equation for particle transport prior to jamming is then

$$\frac{1}{t_f}\frac{\partial}{\partial t}[h_{\rm tot}\langle\phi\rangle] + \frac{1}{r}\frac{\partial}{\partial r}[r h_{\rm tot}\langle u\phi\rangle] = 0. \tag{38}$$

As evaporation progresses, we may start to see surface jamming near the contact line. At this stage we can look at the full 2D mass balance:

$$\frac{1}{t_f}\frac{\partial \phi}{\partial t} + \nabla\cdot\boldsymbol{J} = 0, \tag{39}$$

with the flux term $\boldsymbol{J} = (J_r, J_z)$ being

$$\boldsymbol{J} = \left[\boldsymbol{u}\phi - \frac{1}{\epsilon^2{\rm Pe}}\frac{\partial\phi}{\partial z}\boldsymbol{e}_z\right]\Theta(b-z) + \frac{1}{t_f}\frac{\partial(h_{\rm tot})}{\partial t}\boldsymbol{e}_z\phi_c\Theta(z-b). \tag{40}$$

Integrating up to the free surface $z = h_{\rm tot} > b$, we obtain via the Leibniz rule

$$\begin{aligned}
0 &= \int_0^{h_{\rm tot}}\left\{\frac{1}{t_f}\frac{\partial\phi}{\partial t} + \nabla\cdot\boldsymbol{J}\right\}dz \\
&= \frac{1}{t_f}\frac{\partial}{\partial t}[h_{\rm tot}\langle\phi\rangle] - \frac{1}{t_f}\frac{\partial h_{\rm tot}}{\partial t}\phi\bigg|_{z=h_{\rm tot}} + J_z\bigg|_{z=h_{\rm tot}} + \frac{1}{r}\frac{\partial}{\partial r}\left(r\int_0^{h_{\rm tot}} J_r\,dz\right) - \frac{\partial h_{\rm tot}}{\partial r}J_r\bigg|_{z=h_{\rm tot}} \\
&= \frac{1}{t_f}\frac{\partial}{\partial t}[h_{\rm tot}\langle\phi\rangle] + \frac{1}{r}\frac{\partial}{\partial r}[r h_{\rm tot}\langle u\phi\rangle] - \left(\frac{1}{t_f}\frac{\partial h_{\rm tot}}{\partial t} + \frac{\partial h_{\rm tot}}{\partial r}u\right)\phi\bigg|_{z=h_{\rm tot}} + \frac{1}{t_f}\frac{\partial h_{\rm tot}}{\partial t}\phi_c.
\end{aligned} \tag{41}$$

All terms in the final line cancel since $\phi = \phi_c$ and $u = 0$ in the surface layer. Replacing $h_{\rm tot}\langle u\phi\rangle$ with $b\langle u\phi\rangle_b$, we obtain

$$\frac{1}{t_f}\frac{\partial}{\partial t}[h_{\rm tot}\langle\phi\rangle] + \frac{1}{r}\frac{\partial}{\partial r}[r b\langle u\phi\rangle_b] = 0. \tag{42}$$

This will be one of the component equations in our system. We can use this expression to find a global solute conservation condition analogous to Eq. (24) in the surface capture limit. Since the

solute does not evaporate, we have

$$0 = \frac{d}{dt}\left\{\int_0^l r h_{\text{tot}}\langle\phi\rangle\, dr + \int_0^t |\phi_c H l \dot{l}|(t')\, dt'\right\}$$

$$= \dot{l} l h_{\text{tot}}\langle\phi\rangle|_{r=l} + \int_0^l r\frac{\partial}{\partial t}(h_{\text{tot}}\langle\phi\rangle)\, dr + |\phi_c H l \dot{l}|$$

$$\longrightarrow \dot{l} = -\left.\frac{t_f b\langle ub\rangle_b}{H\phi_c - h_{\text{tot}}\langle\phi\rangle}\right|_{r=l^-} = -\left.\frac{t_f\langle u\phi\rangle_b}{\phi_c - \langle\phi\rangle_b}\right|_{r=l^-}. \tag{43}$$

The shock propagation has been obtained from the last line using Eq. (42) and noting that $h_{\text{tot}} = H$ and $h_{\text{tot}}\langle\phi\rangle = \phi_c(H-b) - b\langle\phi\rangle_b$ at $r = l$. Note that in the limit of large ϵ^2Pe, in which $\phi = \phi_0$ for $z < b$, we recover expression (24), as expected. Based on the findings of the previous section, before surface jamming we will assume a diffusive boundary layer structure of the form

$$\phi = \phi_0 + (\bar{\phi}(r,t) - \phi_0)\exp[-\epsilon^2 \text{Pe} J_{\text{evap}}(h_{\text{tot}} - z)]. \tag{44}$$

The additional degree of freedom offered by the prefactor $\bar{\phi}$ is calculated according to the solute mass conservation condition. Once jamming has occurred at the surface, $\bar{\phi}$ will be fixed at ϕ_c and b will become the adjustable parameter instead. Rather than evolving b at the same rate as the free surface, we solve for it (again, using solute mass conservation) via the expression below:

$$\phi = \begin{cases} \phi_0 + (\phi_c - \phi_0) \\ \quad \times \exp\left(-\frac{\phi_c}{\phi_c - \phi_0}\epsilon^2 \text{Pe} J_{\text{evap}}(b - z)\right), & z < b \\ \phi_c, & b < z < h_{\text{tot}}. \end{cases} \tag{45}$$

Although these expressions mimic the asymptotic result for large ϵ^2Pe, they also become the desired vertically uniform distribution when $\epsilon^2 \text{Pe} \ll 1$. Thus, we expect this interpolation to be consistent with both asymptotic limits. Though in principle it is possible to calculate the depth average of the product $u\phi$ using their known z dependencies, this is cumbersome and assumes in any case that u is independent of the local solute concentration. We will therefore assume that

$$\langle u\phi\rangle_g \approx \langle u\rangle_g\langle\phi\rangle_g, \tag{46}$$

where here g represents either the free surface height or the height of the bottom of the jammed surface layer depending on whether it has formed yet. Of course, expression (46) becomes exact in the vertically homogeneous and surface capture limits. Refer to Appendix B for the numerical solution methodology. To validate our averaging assumption as well as the diffusive boundary layer expression in the context of an axisymmetric drop, simulations of the full 2D advection-diffusion problem wherein ϕ_0/ϕ_c is small were performed using the finite element library OOMPH-LIB [48] (details of these simulations can be found in Appendix A). In the absence of particle jamming, our interpolation model can be solved analytically using the method of characteristics. The depth-averaged solute volume fraction is [32]

$$\langle\phi\rangle = \phi_0\frac{(1-t)^{-1/2} - r^2}{1 - r^2} \tag{47}$$

for kinetic evaporation, and [32]

$$\langle\phi\rangle = \phi_0(1-t)^{-1/4}(1-r^2)^{-1/2}\{1 - [1 - (1-r^2)^{3/2}](1-t)^{3/4}\}^{1/3} \tag{48}$$

for diffusive evaporation. The prefactor $\bar{\phi}$ and thus the full solute concentration field can be inferred by depth-averaging equation (44). In Figs. 6 and 7 we have compared the diffusive boundary layers from full 2D simulations to those predicted by the characteristic solutions for kinetic and diffusive evaporation, respectively. The profiles are taken at $t = 0.3$, which allows time for ϕ to relax towards the similarity form from the initial condition. We find good agreement in the kinetic and diffusive

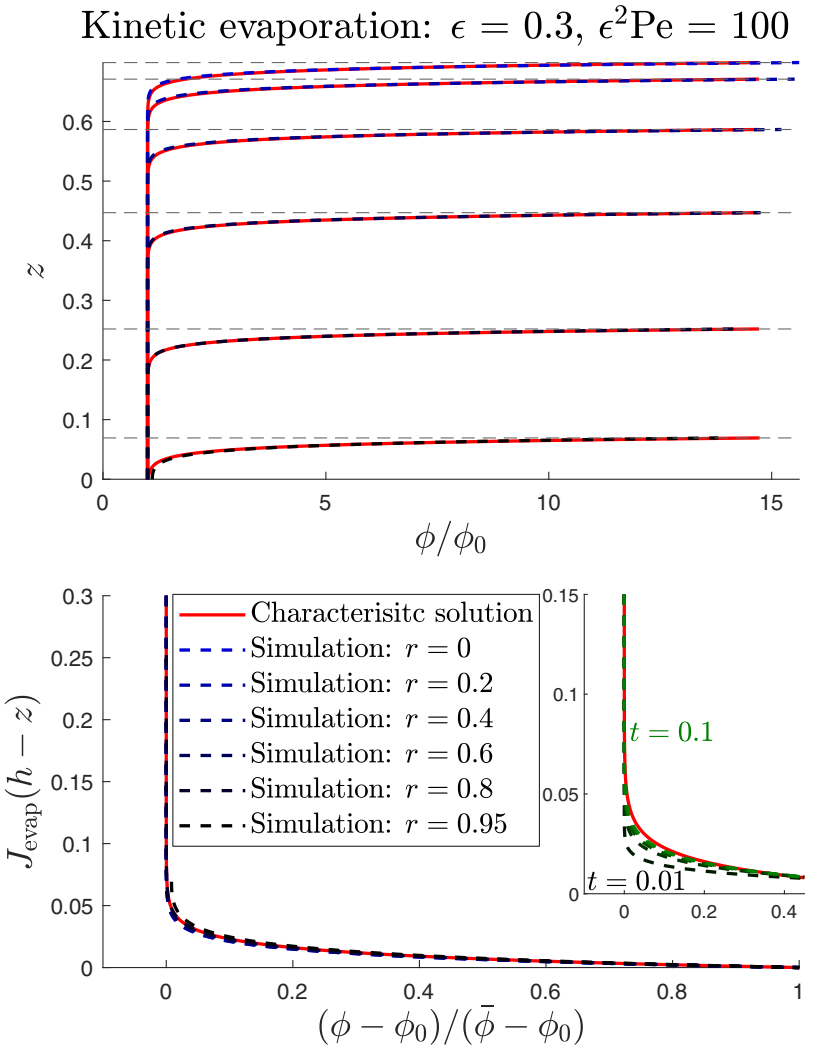

FIG. 6. Comparisons of the diffusive boundary layer in the kinetic evaporation regime for radii ranging from $r = 0$ to $r = 0.95$ at $t = 0.3$. Shown in red is characteristic solution (47). Black-blue curves are obtained from direct simulation. $\bar{\phi}$ is the value of ϕ at the free surface, obtained either from simulation or by depth-averaging equation (44) and using the known characteristic solution. All particle jamming effects are neglected. In the lower panel, axes are appropriately scaled to show collapse onto a single curve as predicted by the solution ansatz. In the inset, we show relaxation towards the solution ansatz over uniform time increments from $t = 0.01$ to $t = 0.1$. All particle jamming effects are neglected.

evaporation regimes across a range of radii from $r = 0$ to $r = 0.95$, despite the fact that radial variations in J_{evap} not being factored in to our diffusive boundary layer expression (though this likely explains why the discrepancy is largest towards the contact line, where J_{evap} diverges, in the case of diffusive evaporation).

Recent work by Ramírez-Soto and Karpitschka [49] has pointed to the importance of Taylor dispersion in the modeling of multicomponent drying droplets. Since no vertical averaging has been done to obtain the numerical results in Figs. 6 and 7, Taylor dispersion is naturally accounted for. Thus, the fact that a good agreement is still observed when compared to our ansatz justifies our neglecting Taylor dispersion in our model development.

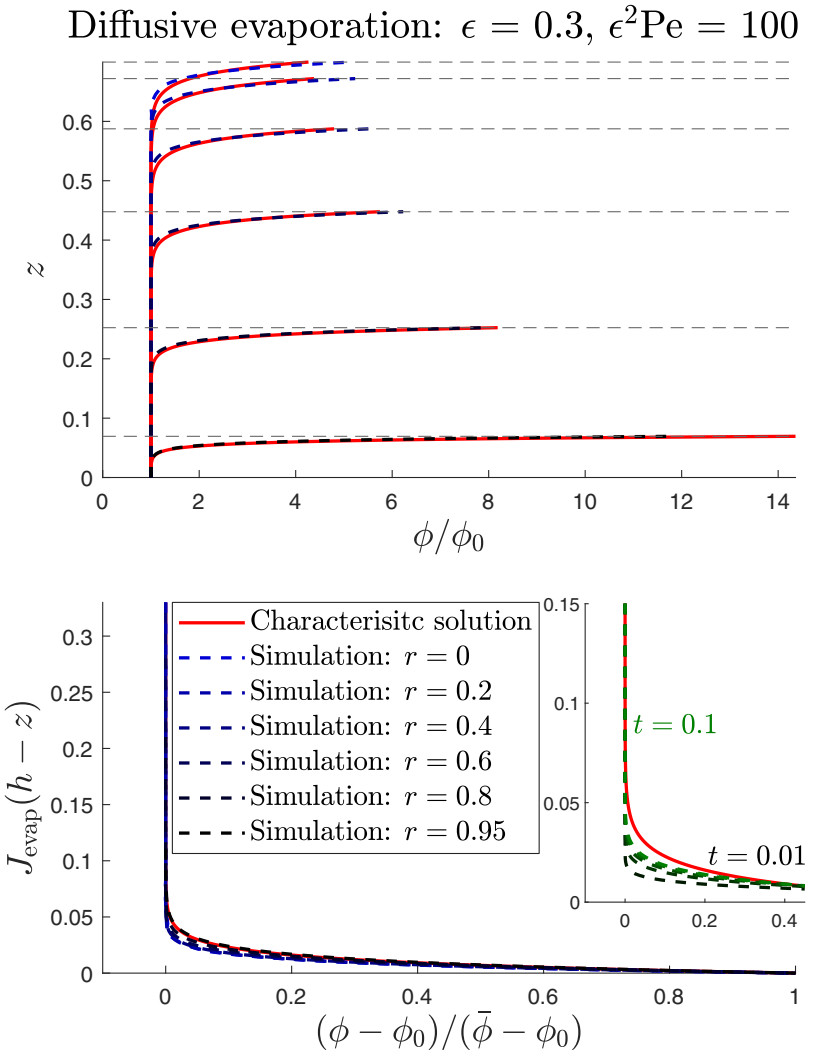

FIG. 7. Comparisons of the diffusive boundary layer in the diffusive evaporation regime for radii ranging from $r = 0$ to $r = 0.95$ at $t = 0.3$. Shown in red is characteristic solution (48). Black-blue curves are obtained from direct simulation. $\bar{\phi}$ is the value of ϕ at the free surface, obtained either from simulation or by the depth-averaging equation (44) and using the known characteristic solution. In the lower panel, axes are appropriately scaled to show collapse onto a single curve as predicted by the solution ansatz. In the inset, we show relaxation towards the solution ansatz over uniform time increments from $t = 0.01$ to $t = 0.1$. All particle jamming effects are neglected.

V. RESULTS

Our results are organized as follows: In Sec. V A we compare our 1D interpolation model (including its limits discussed above) with the experimental findings of Li *et al.* [26]. An attempt is made to estimate the model parameters based off the supplementary information from this work. Since the models developed here break down at the point of touchdown of either the free surface or jammed surface layer, a full comparison with the dried deposit morphology cannot yet be made. Nonetheless, we can still compare the coffee ring height and shape in the vertically homogeneous limit, as this part of the suspension remains static throughout drying. Also, by the point of touchdown in the

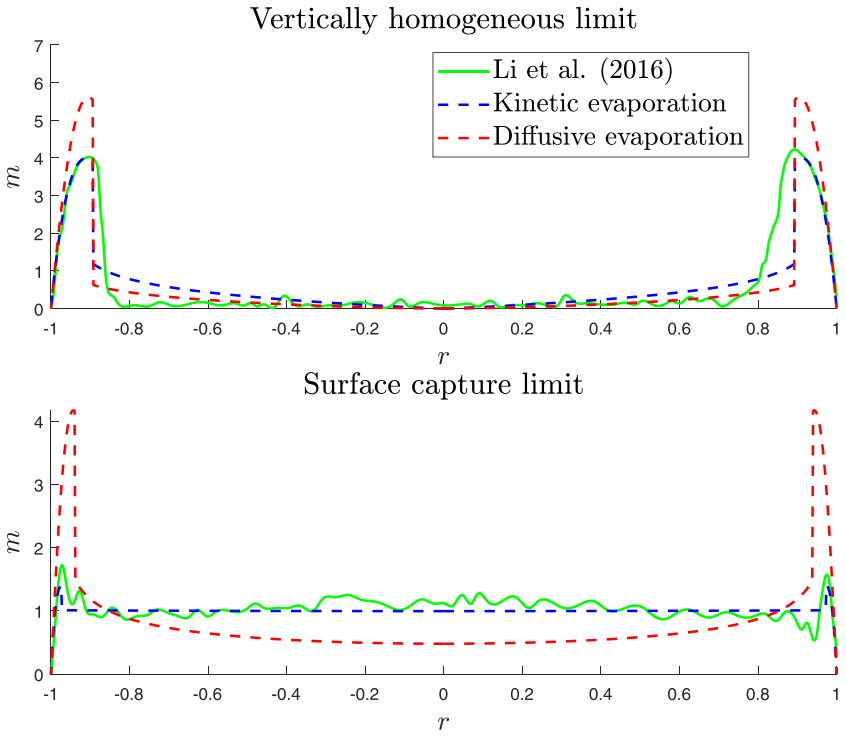

FIG. 8. Comparisons of the vertically homogeneous and surface capture profiles with the experimental results of Li *et al.* [26]. In the vertically homogeneous case, the profiles represent just before film touchdown, whereas in the surface capture limit profiles are taken just before the jammed surface layer meets the substrate. Plots are suitably normalized such that $\int_{-1}^{1} |r| m \, dr = 1$.

surface capture limit almost all solute is part of the coffee ring or jammed surface layer. Therefore, very little change will be seen in the mass profile $h_{\mathrm{tot}}\langle\phi\rangle$ as drying continues.

Following this, in Sec. V B we have conducted a parameteric study to determine which model parameters (or combinations thereof) determine the coffee ring thickness and existence/radial extent of the jammed surface layer.

Finally, in Sec. V C we will analyze the early-time dynamics for both the vertically homogeneous and surface capture limits, deriving scaling laws for the growth of the width, $1 - l$, and height, H, of the deposit region with time. These scaling laws also allow us to predict the variations in $1 - l$ and H as the initial solute volume fraction ϕ_0 is varied. The latter results compare well with numerical results even at late times, beyond their expected validity for early times.

A. Comparisons with experiment

The green profiles shown in Fig. 8 are deposit morphologies reported by Li *et al.* [26] at ambient temperatures of 25 °C (upper plot) and 75 °C (lower plot). For the sake of comparison, we shall suppose that in the former of these there is no surface layer ($\epsilon^2 \mathrm{Pe} \ll 1$) and in the latter a surface layer forms instantaneously ($\epsilon^2 \mathrm{Pe} \gg 1$). This is a reasonable assumption since the Péclet number is temperature-dependent through the evaporation-flux density, $\mathcal{J}^*$, and the solutal diffusion coefficient, D^*, and the net result of these dependencies is that Pe increases monotonically with temperature. Though the initial solute volume fraction was not stated for these particular profiles, we can estimate it from the given information. Since the contact line remains pinned throughout drying, the deposit profiles in each case indicate a contact radius of $R^* = 1.91$ mm. With a quoted

contact angle of $\theta_c = 43^\circ$, the aspect ratio is $\epsilon = \tan(\theta_c/2) = 0.394$, and so we find the initial drop volume (assuming a spherical cap geometry) to be $V^*_{\text{initial}} = \epsilon(3+\epsilon^2)\pi R^{*3}/6 = 4.52\,\text{mm}^3$. Assuming that the deposit remains static when ϕ reaches ϕ_c everywhere, the volume of the deposit then satisfies $\phi_0 V^*_{\text{initial}} = \phi_c V^*_{\text{deposit}}$. This ultimately yields the values $\phi_0 \approx 0.0235$ for the upper plot and $\phi_0 = 0.0193$ for the lower plot. Using these values, we find good agreement in the deposit morphology when compared with the vertically homogeneous and surface capture limits of our model. In particular, we are able to see the transition from coffee ring to uniform deposit with increasing evaporation rates.

In both scenarios the experimental profiles exhibit very strong agreement with the kinetic evaporation model, reproducing both the deposit height and coffee ring thickness. The assumption of diffusive evaporation produces less strong agreement, especially in the surface capture regime in which our model still predicts a strongly enhanced deposit at the contact line. It is surprising that the kinetic profiles should show better agreement, as the drying conditions in the experiments were isothermal with precise humidity controls, ruling out any contributions from thermal convection in the surrounding air (discussed in Sec. II). Under these conditions it is generally assumed that the mode of evaporation is diffusive [50]. Li *et al.* also note the use of surfactants to adhere particles to the drop surface. One could argue that such surfactants would affect only the conditions for particle arrest at the drop surface. If so, since the subsequent growth of the surface layer is determined solely by mass conservation, the final distribution of particles would be unchanged in the limit where the surface layer forms instantly. Nonetheless, since surfactants are not accounted for in our model, the comparison is reduced to a qualitative level. Another reason a full quantitative comparison cannot yet be made is that the theoretical profiles shown here are taken at the point of free surface/jammed surface layer touchdown, at which point there is still solvent yet to evaporate. Progress in resolving this issue (at least in the vertically homogeneous limit) has already been made [41].

The agreement seen here suggests that our simple theoretical treatment of particle jamming at the liquid-air interface, based solely on evaporation kinetics and particle jamming, is sufficient to describe the fundamental physics of the surface capture phenomenon. It is also noteworthy that the surface capture layer observed in our model bears a strong resemblance to the gel layer observed in the experiments of Jalaal *et al.* [51] (see in particular the upper panels of Fig. 5 from this reference).

B. Parametric study of the 1D interpolation model

In the case of a 1D flat interface, it was found that the jamming delay time depends on the two independent system parameters ϕ_0 and $\epsilon^2\text{Pe}$ only through the combination $(\phi_c - \phi_0)/(\phi_0\epsilon^2\text{Pe})$. For instance, if $J_{\text{evap}} = 1$ then no surface layer will form at all if $\epsilon^2\text{Pe} < (\phi_c - \phi_0)/\phi_0$. A natural question is whether this behavior extends to the axisymmetric drop.

Simulations indicate that this combination roughly determines the radial extent of the surface layer when the film touches down, though the final coffee ring width at this stage will depend on the individual choices for ϕ_c and $\epsilon^2\text{Pe}$; see Figs. 9 and 10 for reference. We remind the reader that the discontinuity seen in each of these figures at $r = l(t)$ is an artifact of the model arising from the fact that we have neglected diffusion in the horizontal direction. This modeling choice, however, reflects the relative importance of horizontal and vertical diffusion: Inclusion of the former is likely to make very little difference to our results as the dimensions of the coffee ring are determined primarily through jamming. In Fig. 11 we test our hypothesis further by finding the minimal vertical Péclet number, $(\epsilon^2\text{Pe})_{\text{critical}}$, required for the surface layer to propagate to $r = 0.5$ by the time of touchdown. A good agreement is seen across a range of ϕ_0 values and for both evaporation models. Note that if surface jamming is never achieved, then our model is identical to Popov's (at least concerning the width of the coffee ring and the solute mass per unit area $m \propto h_{\text{tot}}\langle\phi\rangle$). It was found numerically that, for initial dilutions under 10% of ϕ_c, an $\epsilon^2\text{Pe}$ value significantly larger than 1 is usually required to see any surface layer formation. For example, with $\phi_c/\phi_0 = 20$ no surface layer was seen for $\epsilon^2\text{Pe} \lesssim 37$ under kinetic evaporation or $\epsilon^2\text{Pe} \lesssim 92$ under diffusive evaporation. Since m is typically the quantity of interest in CRE modeling as it reflects dried deposit morphology,

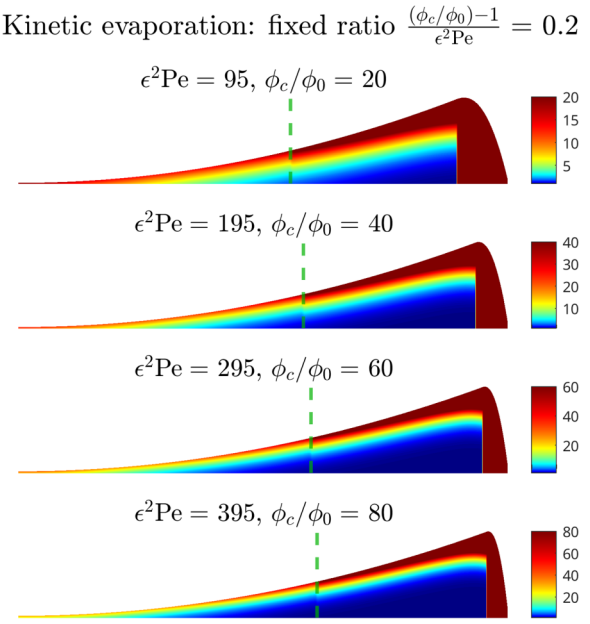

FIG. 9. Color maps showing the progression of the jammed surface layer for a variety of ϕ_0 and $\epsilon^2\mathrm{Pe}$ values such that the ratio $[(\phi_c/\phi_0) - 1]/\epsilon^2\mathrm{Pe}$ is held constant at 0.2. A kinetic evaporation model is used. The color scale has been suitably set so that the diffusive boundary layers are visible. The vertical green dashed line shows the radial position of the jammed surface layer at the point of film touchdown.

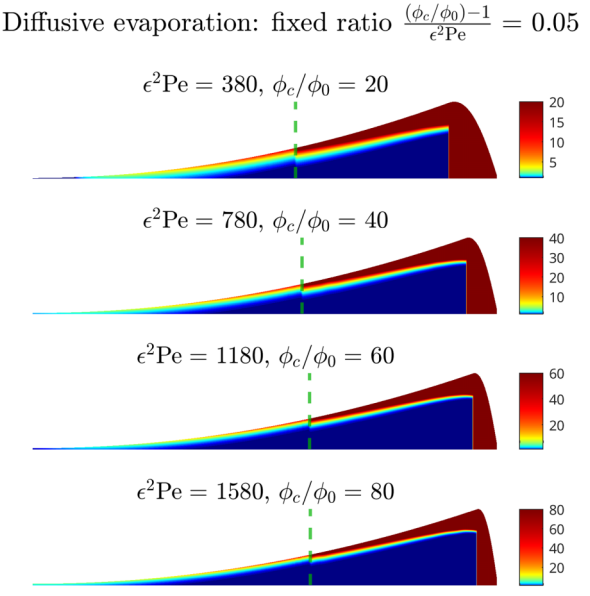

FIG. 10. Color maps showing the progression of the jammed surface layer for a variety of ϕ_0 and $\epsilon^2\mathrm{Pe}$ values such that the ratio $[(\phi_c/\phi_0) - 1]/\epsilon^2\mathrm{Pe}$ is held constant at 0.1. A diffusive evaporation model is used. The color scale has been suitably set so that the diffusive boundary layers are visible. The vertical green dashed line shows the radial position of the jammed surface layer at the point of film touchdown.

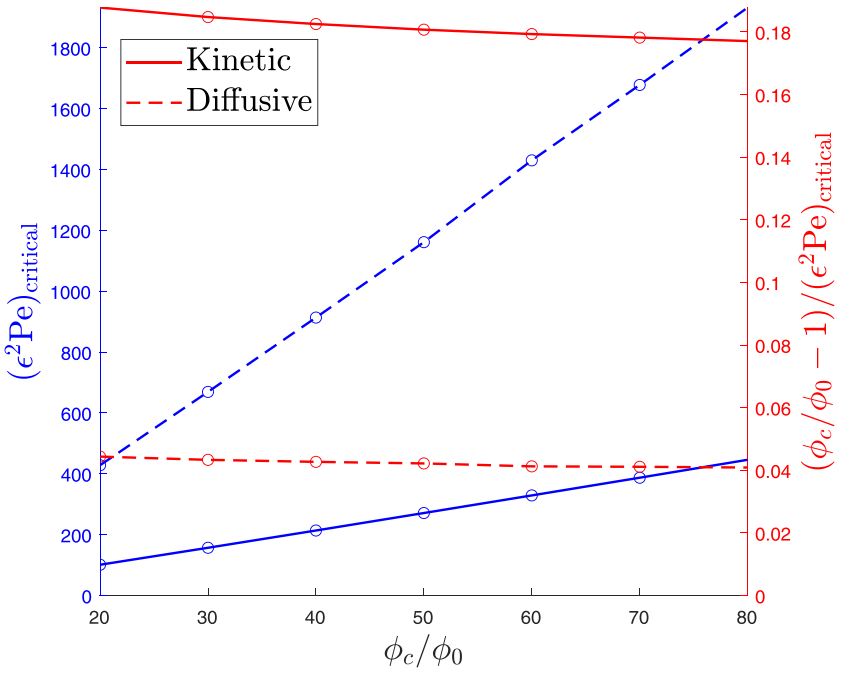

FIG. 11. The minimum vertical Péclet number, $(\epsilon^2\mathrm{Pe})_{\mathrm{critical}}$, required for the jammed surface layer to propagate to $r = 0.5$ by the point of film touchdown. On the right axis, we have additionally plotted $[(\phi_c/\phi_0) - 1]/(\epsilon^2\mathrm{Pe})_{\mathrm{critical}}$ to demonstrate that this ratio remains roughly constant as ϕ_c/ϕ_0 is increased. Solid and dashed lines correspond to kinetic and diffusive evaporation respectively.

this suggests that the assumption of vertical homogeneity commonly used in coffee ring literature may be applicable for $\epsilon^2\mathrm{Pe} \sim 1$ and even larger values. A similar conclusion was made recently by Larsson and Kumar in a study of 1D thin films with infinite extent [21].

We have additionally plotted regime diagrams in Fig. 12 to indicate how far across the drop surface the jammed surface layer is expected to propagate for a given pair of ϕ_c/ϕ_0 and $\epsilon^2\mathrm{Pe}$ values (the dashed white lines in these diagrams correspond to propagation to $r = 0.5$). Interestingly, the intermediate region, in which there is a jammed surface layer that does not reach $r = 0$, is wider for diffusive evaporation than for kinetic evaporation. This is due to the fact that the value of $\epsilon^2\mathrm{Pe}J_{\mathrm{evap}}$ decreases near the center of the drop in the diffusive case, meaning the sharpness of the diffusive boundary layer as described by Eq. (44) will decrease, and so the jammed surface layer is less likely to cover the entire drop surface.

C. Scaling laws and dynamics at early times

At early times, one can derive scaling laws to determine the growth of the width and height of the coffee ring deposit in both the vertically homogeneous and surface capture regimes. To do so, we will look at the initial perturbations $l = 1 - l'$, $H = H'$ and $A = 1 - A'$, where l', H' and A' are small. It is then readily found from Eq. (12) that $H' = 2l'$, and so the deposit region initially grows as a triangular wedge, regardless of the regime we are in (i.e., vertically homogeneous or surface capture) or evaporation model we are using.

Following the arguments of Deegan [44] and Popov [19], we begin by deriving scaling laws in the vertically homogeneous regime. Letting $r_0(t)$ denote the initial coordinate of a particle reaching

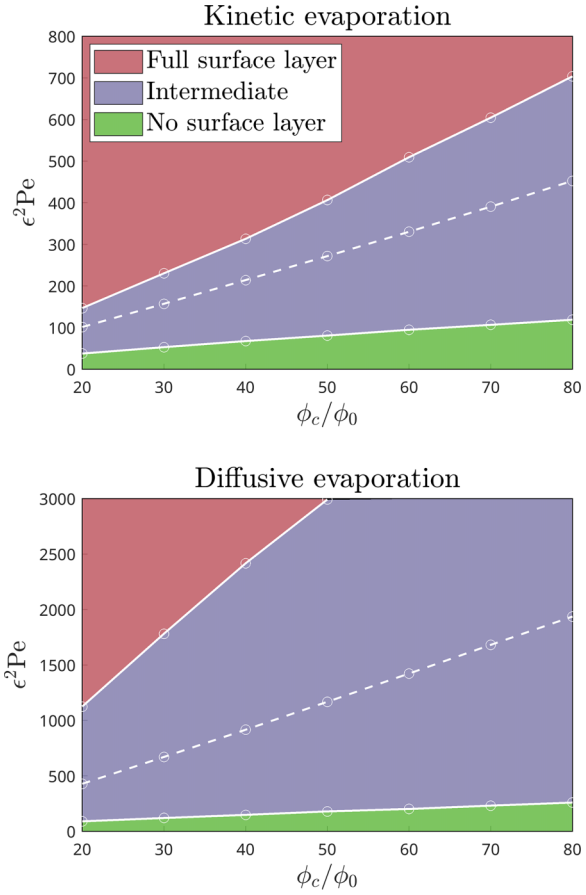

FIG. 12. Regime diagrams indicating the radial extent of the surface layer by the time of touchdown. The red, purple, and green regions correspond to a fully propagated, partially propagated, and no surface layer, respectively. The dashed white line in each diagram corresponds to the surface layer reaching $r = 0.5$ (these lines are also shown in Fig. 11).

the jammed region at time t, it is clear from solute mass conservation that

$$V_D(t) = \phi_0 \int_{r_0(t)}^{1} r h_{\text{tot}}(r, 0)\, dr = \frac{\phi_0}{4}\left(1 - r_0^2\right)^2,$$

where $V_D(t)$ is the volume of solute in the deposit at time t (omitting the 2π prefactor). We may determine $r_0(t)$ by looking at particle trajectories, $\varphi(t)$, which evolve according to $\partial_t \varphi = \langle u \rangle(\varphi(t), t)$. Taking $l \sim 1$ in Eq. (16) gives

$$\frac{\partial \varphi}{\partial t} = \begin{cases} \frac{1}{4}\frac{\varphi}{1-t}, & \text{kinetic evaporation,} \\ \frac{1}{4}\frac{(1-\varphi^2)^{-1/2} - (1-\varphi^2)}{\varphi(1-t)}, & \text{diffusive evaporation.} \end{cases} \tag{49}$$

Solving each of these expressions gives $\varphi(t) = \varphi(0)(1-t)^{-1/4}$ in the kinetic regime and $1 - (1-\varphi(t)^2)^{3/2} = [1 - (1-\varphi(0)^2)^{3/2}](1-t)^{-3/4}$ in the diffusive regime. The coordinate r_0 is then found by setting $\varphi(t) = l \sim 1$ and $\varphi(0) = r_0(t)$, so that

$$r_0(t) = \begin{cases} (1-t)^{1/4}, & \text{kinetic evaporation,} \\ \{1 - [1 - (1-t)^{3/4}]^{2/3}\}^{1/2}, & \text{diffusive evaporation.} \end{cases} \tag{50}$$

Since the deposit region initially grows as a triangular wedge, its volume is $V_D(t) = \phi_c H' l'/2 = \phi_c l'^2$ (again omitting the 2π prefactor). We can thus use the expressions above to find the dynamics of l' at early times. To leading order in t, we find that

$$l' \approx \begin{cases} \frac{1}{4}\sqrt{\frac{\phi_0}{\phi_c}}t, & \text{kinetic evaporation,} \\ \frac{3^{2/3}}{2^{7/3}}\sqrt{\frac{\phi_0}{\phi_c}}t^{2/3}, & \text{diffusive evaporation.} \end{cases} \tag{51}$$

The $\sqrt{\phi_0/\phi_c}t^{2/3}$ dependence was first derived by Deegan [44] and was found to agree with experimental findings within the margins of experimental error. We will now look at the surface capture regime. In this limit the thickness of the jammed surface layer is known analytically, and so it is easier to find the early time dependence for l'. Appealing to the shock propagation condition (24) as well as Eq. (23), we find

$$\begin{aligned} \dot{l} &= -\frac{\phi_0}{\phi_c - \phi_0}\frac{t_f}{H - \frac{\phi_0}{\phi_c-\phi_0}t_f J_{\text{evap}} t} h_{\text{tot}}\langle u\rangle|_{r=l} \\ \longrightarrow \dot{l}' &\approx \frac{\phi_0}{\phi_c - \phi_0} t_f \begin{cases} \frac{l'}{2l' - [\phi_0/(\phi_c-\phi_0)]t_f t}, & \text{kinetic evaporation,} \\ \frac{l'}{(2l')^{3/2} - [\phi_0/(\phi_c-\phi_0)]t_f t/2}, & \text{diffusive evaporation.} \end{cases} \end{aligned} \tag{52}$$

These are solved via the following power-law expressions:

$$l' \approx \begin{cases} \frac{1}{2}\frac{\phi_0}{\phi_c-\phi_0}t, & \text{kinetic evaporation,} \\ \frac{1}{2}\left(\frac{\phi_0}{\phi_c-\phi_0}t\right)^{2/3}, & \text{diffusive evaporation.} \end{cases} \tag{53}$$

Interestingly, although the same time dependence is found in both the vertically homogeneous and surface capture limits for a given evaporation model, the dependence on ϕ_c/ϕ_0 is different. It is natural to ask whether the dependence of l on ϕ_c/ϕ_0 can be inferred, at least up to an arbitrary scale factor, from expressions (51) and (53). In Fig. 13 we show this to be the case: providing the ratio ϕ_c/ϕ_0 is large enough, the scaling relation at late times ($t = 0.8$ shown here) is still as predicted by the early time power law, though the prefactor is different (note that the x axes for these plots are ϕ_c/ϕ_0 rather than $\phi_c/\phi_0 - 1$, though the difference is negligible when this ratio is sufficiently large). The same scaling relations were also found to hold for the deposit height H.

VI. DISCUSSION

We have studied the combined effects of particle jamming and surface capture in evaporating particle suspensions through a simple 1D modeling framework. One key modeling assumption we have made is that particles forming a jammed surface layer move with the free surface, but are not advected any further by the fluid flow. This assumption is contrary to other existing theoretical frameworks used to describe surface capture [30,31], in which there is no jamming so particles that adhere to the free surface are still advected along the surface towards the contact line. It should be emphasized that our assumption, which arises naturally with the inclusion of jamming, is crucial to qualitatively reproduce the deposit morphology seen experimentally by Li *et al.* [26] at high evaporation rates. In particular, under kinetic evaporation our model predicts a a deposit which is uniform everywhere except very close to the contact line in the limit $\epsilon^2\text{Pe} \gg 1$.

For intermediate values of $\epsilon^2\text{Pe}$, we have proposed a diffusive boundary layer expression to specify the z dependence of the solute volume fraction *a priori*. We find that our expression agrees well with direct simulations of the full advection-diffusion problem when ϕ_c/ϕ_0 is large (the dilute limit), though further verification of our modified expression for once a surface layer has formed is needed. One of three possible outcomes emerge in our simulations of the 1D interpolation model:

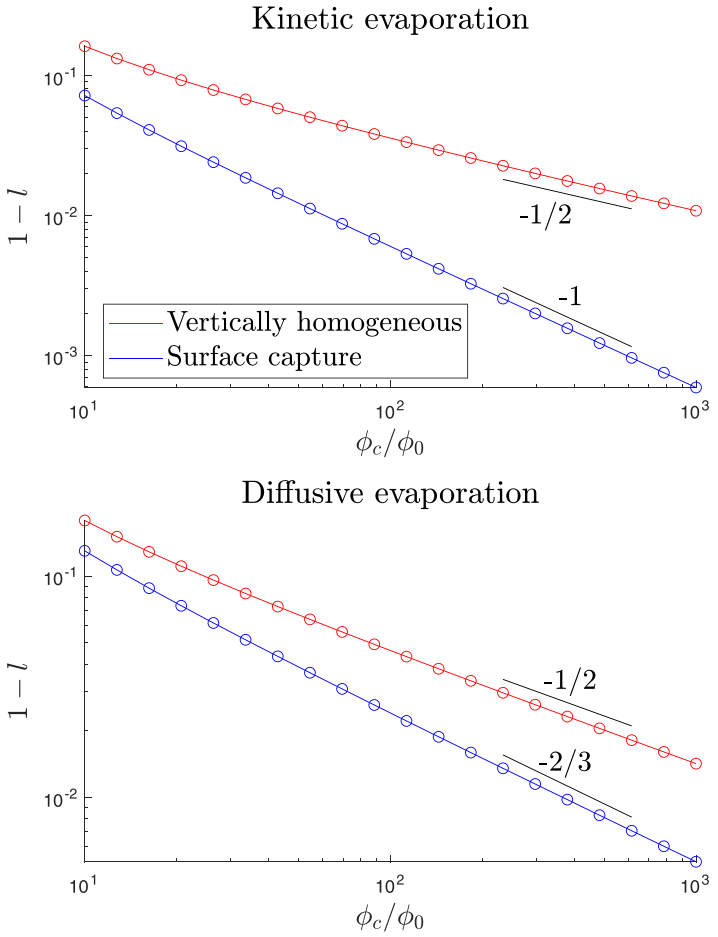

FIG. 13. Doubly logarithmic plots of the deposit width $1-l$ as a function of ϕ_c/ϕ_0 for both the kinetic and diffusive evaporation regimes. Red plots represent the vertically homogeneous limit, and blue plots represent the surface capture limit. Each plot point shown corresponds to a simulation terminated at $t = 0.8$. To demonstrate agreement with Eqs. (51) and (53) up to a scale factor, black lines with gradients $-1/2$, -1, and $-2/3$ are also shown.

(1) There is no surface layer formation. In this case, the predictions of our model for the solute mass per unit area $m \propto h\phi$ are identical to those predicted by Popov's model.

(2) A surface layer forms, but only propagates part way across the drops surface.

(3) A surface layer forms and spans the entire free surface.

Interestingly, outcome 1 can happen even for $\epsilon^2\mathrm{Pe}$ considerably larger than unity. This suggests that the vertical averaging approximation, which is of widespread use in CRE modeling, is valid beyond the regime $\epsilon^2\mathrm{Pe} \ll 1$ providing we are interested only in the deposit morphology at the end of evaporation. Depending on the outcome, we can run out simulations until either the free surface or the jammed surface layer meets the substrate at $r = 0$. In the vertically homogeneous limit, this is not such an issue as by this stage most of the solute is part of the coffee ring deposit. However, the surface capture profiles are clearly incomplete.

In future work we aim to lift this modeling restriction by tracking all jammed particle fronts implicitly. This technique will be outlined and implemented in a related article [41] for the vertically homogeneous case. In that work we will demonstrate that simulations can be continued until the

solute has jammed everywhere (and thus no more deformation can occur since the suspension is incompressible everywhere) and that extension to arbitrary contact sets can be easily achieved using the finite element method.

Finally, we note that since the primary aim of this work was to make the minimal adjustments to Popov's model to account for surface capture, the Marangoni effect, either solutal or thermal, has been neglected throughout. Though our study has been restricted to a single component fluid laden with particles, binary fluids can exhibit complex dynamics as a result of the Marangoni effect. For instance, inward directed solutal Marangoni flow, such as that observed by Thayyil Raju *et al.* [52] in water-glycerol droplets, can lead to the formation of a secondary cluster of particles, termed the Marangoni ring, which forms just below the air-liquid interface at a radial position near the contact line. Outward Marangoni flow may, however, be more relevant to the surface capture effect described here; in particular, it was found by Bruning *et al.* [53] in a study of evaporating salty droplets that this flow initiates surface layer formation under conditions where a surface layer would otherwise not be observed. Therefore, accounting for multicomponent fluids could be a natural direction for generalization of the model.

The data that support the findings of this study are openly available in figshare at [54].

ACKNOWLEDGMENTS

This work was supported by the EPSRC under Grants No. EP/W031426/1, No. EP/S029966/1, and No. EP/P031684/1.

APPENDIX A: NUMERICAL METHOD: 2D ADVECTION-DIFFUSION SIMULATION IN THE DILUTE LIMIT

For direct simulation of the solute transport problem with jamming effects omitted, we solved the axisymmetric advection-diffusion equation with a prescribed underlying velocity field $\boldsymbol{u} = u\boldsymbol{e}_r + w\boldsymbol{e}_z$:

$$\frac{1}{t_f}\frac{\partial \phi}{\partial t} + \frac{1}{r}\frac{\partial}{\partial r}\left[r\left(u\phi - \frac{1}{\mathrm{Pe}}\frac{\partial \phi}{\partial r}\right)\right] + \frac{\partial}{\partial z}\left(w\phi - \frac{1}{\epsilon^2 \mathrm{Pe}}\frac{\partial \phi}{\partial z}\right) = 0. \tag{A1}$$

Under the lubrication approximation, the field $\boldsymbol{u}$ can be inferred from the depth average $\langle u\rangle$ and the incompressibility condition. In the kinetic evaporation regime we have

$$u = \frac{3r}{4(1-t)}\frac{z}{h}\left(2 - \frac{z}{h}\right), \quad w = \frac{3}{2}\left[-\left(\frac{z}{h}\right)^2 + \frac{1+r^2}{3}\left(\frac{z}{h}\right)^3\right], \tag{A2}$$

and in the diffusive evaporation regime

$$\begin{aligned} u &= \frac{3}{4(1-t)r}[(1-r^2)^{-1/2} - (1-r^2)]\frac{z}{h}\left(2 - \frac{z}{h}\right), \\ w &= -\frac{9}{4}(1-r^2)^{-1/2}\left(\frac{z}{h}\right)^2 + \left[\frac{5}{4}(1-r^2)^{-1/2} - \frac{1}{2}(1-r^2)\right]\left(\frac{z}{h}\right)^3. \end{aligned} \tag{A3}$$

Equation (A1) is subject to the no-flux boundary conditions:

$$\frac{\partial \phi}{\partial r} = 0, \quad r = 0, \tag{A4a}$$

$$\frac{\partial \phi}{\partial z} = 0, \quad z = 0, \tag{A4b}$$

$$\left[\frac{1}{t_f}\frac{\partial \phi}{\partial t} + u\frac{\partial h}{\partial r} - w\right]\phi - \frac{1}{\mathrm{Pe}}\frac{\partial h}{\partial r}\frac{\partial \phi}{\partial r} + \frac{1}{\epsilon^2 \mathrm{Pe}}\frac{\partial \phi}{\partial z} = 0, \quad z = h(r,t) = (1-t)(1-r^2). \tag{A4c}$$

In order to resolve compatibility issues arising between the advection term derived from the lubrication equations and the governing PDE, an additional vertical boundary is added at $r = 1 - \delta$ (where $\delta = 0.005$) over which no flux is applied. When Pe is large, this merely changes the position of the sharp radial diffusive boundary layer. As long as the coordinates of interest (i.e., the sample r values in Figs. 6 and 7) are far enough away from the contact line, the value of δ used does not matter.

Since the mesh conforms to the free surface of the drop, the nodal positions also change throughout the simulation. When calculating time derivatives this change is accounted for using the arbitrary Lagrangian-Eulerian (ALE) relation:

$$\left.\frac{\partial \phi}{\partial t}\right|_{\text{Eulerian}} = \left.\frac{d}{dt}\right|_{\text{node}} \phi - \boldsymbol{v}_{\text{mesh}} \cdot \nabla \phi, \tag{A5}$$

where $(\partial\phi/\partial t)|_{\text{node}}$ is evaluated using the history of values at the node at its previous positions, and $\boldsymbol{v}_{\text{mesh}}$ is the local mesh velocity.

The equations were discretized and solved using the finite element library OOMPH-LIB [48]. The computational mesh was formed of nine-node quadrilateral elements, and adaptive quad-tree refinement was used to resolve the sharp diffusive boundary layer. Time integration was performed using the BDF2 timestepping scheme.

APPENDIX B: NUMERICAL METHOD: 1D INTERPOLATION MODEL

For the 1D interpolation model introduced in Sec. IV C, Eqs. (12), (15), (42), (43), and (44) or (45), depending on whether or not a jammed surface layer has formed, comprise the system to be solved numerically. The advection problem is solved on the contracting domain $r \in [0, l(t)]$ using the ALE relation to evaluate time derivatives:

$$\frac{1}{tf}\left[\frac{d}{dt} - \dot{r}_j \frac{\partial}{\partial r}\right](h_{\text{tot}}\langle\phi\rangle)|_j + \frac{1}{r_j}\frac{1}{r_j - r_{j-1}}[rb\langle u\rangle_b\langle\phi\rangle_b]_{j-1}^{j} = 0, \quad \dot{r}_j = r_j\dot{l}/l. \tag{B1}$$

Here the notation $[\cdot]_{j-1}^{j}$ refers to the difference in values at nodes j and $j-1$. The unknown prefactor $\bar{\phi}$ was calculated internally at each time step using its relation to the depth-averaged concentration:

$$\langle\phi\rangle = \phi_0 + \frac{\bar{\phi} - \phi_0}{\epsilon^2 \text{Pe} J_{\text{evap}} h_{\text{tot}}}[1 - \exp(-\epsilon^2 \text{Pe} J_{\text{evap}} h_{\text{tot}})]. \tag{B2}$$

If at a given position r, $\bar{\phi}$ is found to be greater than ϕ_c, then we are in the post-jamming regime. A smoothing parameter method is used to interpolate the update equation for b between the two regimes:

$$\frac{\partial b}{\partial t} = \left(\frac{\partial b}{\partial t}\right)^{-}\Theta_\delta\left(\frac{\phi_c - \bar{\phi}}{\phi_0}\right) + \left(\frac{\partial b}{\partial t}\right)^{+}\Theta_\delta\left(\frac{\bar{\phi} - \phi_c}{\phi_0}\right), \tag{B3}$$

where

$$\left(\frac{\partial b}{\partial t}\right)^{-} = \dot{A}(l^2 - r^2), \tag{B4a}$$

$$\left(\frac{\partial b}{\partial t}\right)^{+} = \frac{\partial_t[h_{\text{tot}}(\phi_c - \langle\phi\rangle)]}{(\phi_c - \phi)\left[1 - \exp\left(-\frac{\phi_c}{\phi_c - \phi_0}\epsilon^2 \text{Pe} J_{\text{evap}}\right)\right]}. \tag{B4b}$$

Expression (B4a) follows directly from Eqs. (11) and (12), while expression (B4b) can be derived by integrating Eq. (45) up to the free surface and taking a time derivative. A tanh approximation of the Heaviside step function is used for Θ_δ:

$$\Theta_\delta(x) = \tfrac{1}{2}[1 + \tanh(x/\delta)]. \tag{B5}$$

After spatial discresization, a first-order ODE system of the form $\dot{\boldsymbol{y}} = f(t, \boldsymbol{y})$, where $\boldsymbol{y} = (l, A, H, \langle\phi\rangle_1, \ldots, \langle\phi\rangle_N, b_1, \ldots, b_N)$ and N is the number of nodes, is obtained. This system was solved implicitly using ode15s in MATLAB.

[1] D. Lohse, Fundamental fluid dynamics challenges in inkjet printing, Annu. Rev. Fluid Mech. **54**, 349 (2022).

[2] G. Berteloot, C.-T. Pham, A. Daerr, F. Lequeux, and L. Limat, Evaporation-induced flow near a contact line: Consequences on coating and contact angle, Europhys. Lett. **83**, 14003 (2008).

[3] J. Jing, J. Reed, J. Huang, X. Hu, V. Clarke, J. Edington, D. Housman, T. S. Anantharaman, E. J. Huff, B. Mishra *et al.*, Automated high resolution optical mapping using arrayed, fluid-fixed DNA molecules, Proc. Natl. Acad. Sci. USA **95**, 8046 (1998).

[4] R. D. Deegan, O. Bakajin, T. F. Dupont, G. Huber, S. R. Nagel, and T. A. Witten, Capillary flow as the cause of ring stains from dried liquid drops, Nature (London) **389**, 827 (1997).

[5] H. Gelderblom, C. Diddens, and A. Marin, Evaporation-driven liquid flow in sessile droplets, Soft Matter **18**, 8535 (2022).

[6] H. Yabu and M. Shimomura, Preparation of self-organized mesoscale polymer patterns on a solid substrate: Continuous pattern formation from a receding meniscus, Adv. Funct. Mater. **15**, 575 (2005).

[7] P. C. Kiatkirakajorn and L. Goehring, Formation of shear bands in drying colloidal dispersions, Phys. Rev. Lett. **115**, 088302 (2015).

[8] E. R. Dufresne, E. I. Corwin, N. A. Greenblatt, J. Ashmore, D. Y. Wang, A. D. Dinsmore, J. X. Cheng, X. S. Xie, J. W. Hutchinson, and D. A. Weitz, Flow and fracture in drying nanoparticle suspensions, Phys. Rev. Lett. **91**, 224501 (2003).

[9] L. Pauchard and C. Allain, Buckling instability induced by polymer solution drying, Europhys. Lett. **62**, 897 (2003).

[10] C. Seyfert, E. J. W. Berenschot, N. R. Tas, A. Susarrey-Arce, and A. Marin, Evaporation-driven colloidal cluster assembly using droplets on superhydrophobic fractal-like structures, Soft Matter **17**, 506 (2021).

[11] A. J. Liu and S. R. Nagel, The jamming transition and the marginally jammed solid, Annu. Rev. Condens. Matter Phys. **1**, 347 (2010).

[12] A. G. Marín, H. Gelderblom, D. Lohse, and J. H. Snoeijer, Rush-hour in evaporating coffee drops, Phys. Fluids **23**, 091111 (2011).

[13] F. Parisse and C. Allain, Shape changes of colloidal suspension droplets during drying, J. Phys. II France **6**, 1111 (1996).

[14] F. Parisse and C. Allain, Drying of colloidal suspension droplets: Experimental study and profile renormalization, Langmuir **13**, 3598 (1997).

[15] M. R. Moore, D. Vella, and J. M. Oliver, The nascent coffee ring: How solute diffusion counters advection, J. Fluid Mech. **920**, A54 (2021).

[16] A. F. Routh and W. B. Russel, Horizontal drying fronts during solvent evaporation from latex films, AIChE J. **44**, 2088 (1998).

[17] C. N. Kaplan and L. Mahadevan, Evaporation-driven ring and film deposition from colloidal droplets, J. Fluid Mech. **781**, R2 (2015).

[18] A. W. Wray, D. T. Papageorgiou, R. V. Craster, K. Sefiane, and O. K. Matar, Electrostatic suppression of the "coffee-stain effect", Procedia IUTAM **15**, 172 (2015).

[19] Y. O. Popov, Evaporative deposition patterns: Spatial dimensions of the deposit, Phys. Rev. E **71**, 036313 (2005).
[20] T. Pham and S. Kumar, Drying of droplets of colloidal suspensions on rough substrates, Langmuir **33**, 10061 (2017).
[21] C. Larsson and S. Kumar, Quantitative analysis of the vertical-averaging approximation for evaporating thin liquid films, Phys. Rev. Fluids **7**, 094002 (2022).
[22] A. G. Marín, H. Gelderblom, D. Lohse, and J. H. Snoeijer, Order-to-disorder transition in ring-shaped colloidal stains, Phys. Rev. Lett. **107**, 085502 (2011).
[23] P. J. Yunker, T. Still, M. A. Lohr, and A. G. Yodh, Suppression of the coffee-ring effect by shape-dependent capillary interactions, Nature (London) **476**, 308 (2011).
[24] H. Kim, F. Boulogne, E. Um, I. Jacobi, E. Button, and H. A. Stone, Controlled uniform coating from the interplay of Marangoni flows and surface-adsorbed macromolecules, Phys. Rev. Lett. **116**, 124501 (2016).
[25] T. P. Bigioni, X.-M. Lin, T. T. Nguyen, E. I. Corwin, T. A. Witten, and H. M. Jaeger, Kinetically driven self assembly of highly ordered nanoparticle monolayers, Nat. Mater. **5**, 265 (2006).
[26] Y. Li, Q. Yang, M. Li, and Y. Song, Rate-dependent interface capture beyond the coffee-ring effect, Sci. Rep. **6**, 24628 (2016).
[27] C. T. Burkhart, K. L. Maki, and M. J. Schertzer, Effects of interface velocity, diffusion rate, and radial velocity on colloidal deposition patterns left by evaporating droplets, J. Heat Transfer **139**, 111505 (2017).
[28] K. L. Maki and S. Kumar, Fast evaporation of spreading droplets of colloidal suspensions, Langmuir **27**, 11347 (2011).
[29] V. S. Punati and M. S. Tirumkudulu, Modeling the drying of polymer coatings, Soft Matter **18**, 214 (2022).
[30] S. Jafari Kang, V. Vandadi, J. D. Felske, and H. Masoud, Alternative mechanism for coffee-ring deposition based on active role of free surface, Phys. Rev. E **94**, 063104 (2016).
[31] T. A. H. Nguyen, S. R. Biggs, and A. V. Nguyen, Manipulating colloidal residue deposit from drying droplets: Air/liquid interface capture competes with coffee-ring effect, Chem. Eng. Sci. **167**, 78 (2017).
[32] R. Zheng, A study of the evaporative deposition process: Pipes and truncated transport dynamics, Eur. Phys. J. E **29**, 205 (2009).
[33] M. J. Hertaeg, C. Rees-Zimmerman, R. F. Tabor, A. F. Routh, and G. Garnier, Predicting coffee ring formation upon drying in droplets of particle suspensions, J. Colloid Interface Sci. **591**, 52 (2021).
[34] I. Sneddon, *Mixed Boundary Value Problems in Potential Theory* (North-Holland, Amsterdam, 1966).
[35] F. Carle, S. Semenov, M. Medale, and D. Brutin, Contribution of convective transport to evaporation of sessile droplets: Empirical model, Int. J. Therm. Sci. **101**, 35 (2016).
[36] M. N. Gueye, A. Carella, J. Faure-Vincent, R. Demadrille, and J.-P. Simonato, Progress in understanding structure and transport properties of PEDOT-based materials: A critical review, Prog. Mater. Sci. **108**, 100616 (2020).
[37] G. Rivers (private communication).
[38] National Institute of Standards and Technology, Thermophysical properties of fluid systems (2018), webbook.nist.gov/chemistry/fluid/.
[39] W. Haynes, *CRC Handbook of Chemistry and Physics*, 95th edition (CRC Press, Boca Raton, 2014).
[40] K. Jain, A. Y. Mehandzhiyski, I. Zozoulenko, and L. Wågberg, PEDOT: PSS nano-particles in aqueous media: A comparative experimental and molecular dynamics study of particle size, morphology and z-potential, J. Colloid Interface Sci. **584**, 57 (2021).
[41] N. Coombs, M. Chubynsky, and J. Sprittles (unpublished).
[42] A. Oron, S. H. Davis, and S. G. Bankoff, Long-scale evolution of thin liquid films, Rev. Mod. Phys. **69**, 931 (1997).
[43] D. Brutin, Influence of relative humidity and nano-particle concentration on pattern formation and evaporation rate of pinned drying drops of nanofluids, Colloids Surf. A: Physicochem. Eng. **429**, 112 (2013).
[44] R. D. Deegan, Pattern formation in drying drops, Phys. Rev. E **61**, 475 (2000).
[45] T. Okuzono, K. Ozawa, and M. Doi, Simple model of skin formation caused by solvent evaporation in polymer solutions, Phys. Rev. Lett. **97**, 136103 (2006).

[46] H. Tan, C. Diddens, P. Lv, J. G. M. Kuerten, X. Zhang, and D. Lohse, Evaporation-triggered microdroplet nucleation and the four life phases of an evaporating ouzo drop, Proc. Natl. Acad. Sci. USA **113**, 8642 (2016).

[47] M. R. Moore, D. Vella, and J. M. Oliver, The nascent coffee ring with arbitrary droplet contact set: An asymptotic analysis, J. Fluid Mech. **940**, A38 (2022).

[48] M. Heil and A. Hazel, oomph-lib - An object-oriented multi-physics finite-element library, in *Fluid-Structure Interaction*, edited by M. Schäfer and H.-J. Bungartz, Lecture Notes in Computer Science Vol. 53 (Springer, Berlin, Heidelberg, 2006), pp. 19–49; oomph-lib is available as open-source software at http://www.oomph-lib.org.

[49] O. Ramírez-Soto and S. Karpitschka, Taylor dispersion in thin liquid films of volatile mixtures: A quantitative model for Marangoni contraction, Phys. Rev. Fluids **7**, L022001 (2022).

[50] H. Hu and R. G. Larson, Evaporation of a sessile droplet on a substrate, J. Phys. Chem. B **106**, 1334 (2002).

[51] M. Jalaal, C. Seyfert, B. Stoeber, and N. J. Balmforth, Gel-controlled droplet spreading, J. Fluid Mech. **837**, 115 (2018).

[52] L. Thayyil Raju, C. Diddens, Y. Li, A. Marin, M. N. van der Linden, X. Zhang, and D. Lohse, Evaporation of a sessile colloidal water-glycerol droplet: Marangoni ring formation, Langmuir **38**, 12082 (2022).

[53] M. A. Bruning, L. Loeffen, and A. Marin, Particle monolayer assembly in evaporating salty colloidal droplets, Phys. Rev. Fluids **5**, 083603 (2020).

[54] https://doi.org/10.6084/m9.figshare.24435169.